Front. Optoelectron. 2014, 7(2): 121–155
DOI 10.1007/s12200-013-0371-5

REVIEW ARTICLE

Investigation of ultra-broadband terahertz time-domain spectroscopy with terahertz wave gas photonics

Xiaofei LU[1], Xi-Cheng ZHANG (✉)[2]

1 SunEdison Inc. 501 Pearl Dr. Saint Peters, MO 63376, USA
2 The Institute of Optics, University of Rochester, Rochester, NY 14627-0186, USA

Abstract Recently, air plasma, produced by focusing an intense laser beam to ionize atoms or molecules, has been demonstrated to be a promising source of broadband terahertz waves. However, simultaneous broadband and coherent detection of such broadband terahertz waves is still challenging. Electro-optical sampling and photoconductive antennas are the typical approaches for terahertz wave detection. The bandwidth of these detection methods is limited by the phonon resonance or carrier's lifetime. Unlike solid-state detectors, gaseous sensors have several unique features, such as no phonon resonance, less dispersion, no Fabry-Perot effect, and a continuous renewable nature. The aim of this article is to review the development of a broadband terahertz time-domain spectrometer, which has both a gaseous emitter and sensor mainly based on author's recent investigation. This spectrometer features high efficiency, perceptive sensitivity, broad bandwidth, adequate signal-to-noise ratio, sufficient dynamic range, and controllable polarization.

The detection of terahertz waves with ambient air has been realized through a third order nonlinear optical process: detecting the second harmonic photon that is produced by mixing one terahertz photon with two fundamental photons. In this review, a systematic investigation of the mechanism of broadband terahertz wave detection was presented first. The dependence of the detection efficiency on probe pulse energy, bias field strength, gas pressure and third order nonlinear susceptibility of gases were experimentally demonstrated with selected gases. Detailed discussions of phase matching and Gouy phase shift were presented by considering the focused condition of Gaussian beams. Furthermore, the bandwidth dependence on probe pulse duration was also demonstrated. Over 240 times enhancement of dynamic range had been accomplished with *n*-hexane vapor compared to conventional air sensor. Moreover, with sub-20 fs laser pulses delivered from a hollow fiber pulse compressor, an ultra-broad spectrum covering from 0.3 to 70 THz was also showed.

In addition, a balanced detection scheme using a polarization dependent geometry was developed by author to improve signal-to-noise ratio and dynamic range of conventional terahertz air-biased-coherent-detection (ABCD) systems. Utilizing the tensor property of third order nonlinear susceptibility, second harmonic pulses with two orthogonal polarizations was detected by two separated photomultiplier tubes (PMTs). The differential signal from these two PMTs offers a realistic method to reduce correlated laser fluctuation, which circumvents signal-to-noise ratio and dynamic range of conventional terahertz ABCD systems. A factor of two improvement of signal-to-noise ratio was experimentally demonstrated.

This paper also introduces a unique approach to directly produce a broadband elliptically polarized terahertz wave from laser-induced plasma with a pair of double helix electrodes. The theoretical and experimental results demonstrated that velocity mismatch between excitation laser pulses and generated terahertz waves plays a key role in the properties of the elliptically polarized terahertz waves and confirmed that the far-field terahertz emission pattern is associated with a coherent process. The results give insight into the important influence of propagation effects on terahertz wave polarization control and complete the mechanism of terahertz wave generation from laser-induced plasma.

This review provides a critical understanding of broadband terahertz time-domain spectroscopy (THz-TDS) and introduces further guidance for scientific applications of terahertz wave gas photonics.

Keywords terahertz spectroscopy, terahertz detection, broadband, gas sensor

Received August 14, 2013; accepted October 25, 2013

E-mail: xi-cheng.zhang@rochester.edu

1 Introduction

1.1 Background

The terahertz spectral range, commonly defined from 300 GHz to 10 THz and located between the microwave and far infrared spectral regions, is one of the least-explored parts of electromagnetic spectrum. In the past 20 years, terahertz science and technology have been received increasing attention, triggered by tremendous progress in the development of sources, detectors, optics and systems. Terahertz technology is now growing due to its broad applications, for example in homeland security, biomedicine, material identification, spectroscopy and non-destructive imaging [1–3].

An important technique in the field of terahertz research, particularly for scientific applications, is terahertz time-domain spectroscopy (THz-TDS) [4,5]. Widely applied in material science, THz-TDS is popular because of its unique wavelength, broad bandwidth and ability to extract both amplitude and phase information in single spectroscopic measurement. The principle of THz-TDS is that a time domain measurement is achieved by mixing a pulsed terahertz wave with sampling optical pulses in a detector. The temporal waveform of terahertz waves thus can be obtained by varying the time delay between the optical probe beam and terahertz waves.

In the past two decades, THz-TDS has been broadly applied into material science to investigate vibrational or rotational resonance of materials [5,6]. With the dramatically increasing development of terahertz sources and detectors, there have been numerous recent breakthroughs in the field, which have pushed terahertz research into the center stage. For example, with recently developed intense pulsed terahertz sources [7–11], terahertz spectroscopy extends into the nonlinear region [12–20]. With picosecond time duration, terahertz waves have also been used as a superior probing tool for the low-energy carrier dynamics in various electronic materials [21–23].

1.2 Generation of broadband terahertz waves

Typically, pulsed terahertz waves are generated through optical excitation that requires ultrashort femtosecond lasers. These excitation processes can be grouped into two general categories. One common method employed in the generation of broadband terahertz radiation utilizes nonlinear optical effects, such as second-order nonlinearity: optical rectification. One alternative method uses a photoconductive antenna.

1.2.1 Optical rectification

Optical rectification is one of the approaches to generate pulsed terahertz waves [24]. While using femtosecond laser pulses to interact with an electro-optic medium, terahertz radiation can be produced via a different frequency mixing process. Conventional optical rectification, which was among the first nonlinear optical effects discovered, usually refers to the generation of direct current (DC) or low frequency electric polarization by an intense optical beam in a nonlinear medium. In the optical rectification process for terahertz wave generation, an ultrafast laser pulse in a nonlinear optical medium creates a beating polarization, which may be regarded as the beating of various Fourier components of the driving optical spectrum. Pulsed electromagnetic waves are then radiated by the time varying dielectric polarization that is equivalent to a transient dipole. Zinc-blende crystals are the most commonly used electro-optic crystals for terahertz generation. Terahertz radiation emission has been reported from a variety of nonlinear materials, such as lithium niobate ($LiNbO_3$), lithium tantalate ($LiTaO_3$), zinc telluride (ZnTe), indium phosphide (InP), gallium arsenide (GaAs), gallium selenide (GaSe), cadmium telluride (CdTe), cadmium zinc telluride (CdZnTe), and diethylaminosulfurtetrafluoride (DAST).

Typically, the optical phonon resonances and phase match in the material determine the bandwidth of an electro-optic crystal for terahertz generation. The terahertz frequency generation is not available in the frequency range around phonon absorption bands of a material. Moreover, the phase match of each frequency component requires the thickness of crystal to be within coherent length. The terahertz emission bandwidth increases when the crystal becomes thinner. However, terahertz emission strength of a crystal is proportional to the thickness of the crystal. The terahertz emission strength decreases when the crystal becomes thinner. Han and Zhang reported a higher frequency response of 17 THz from ZnTe crystal limited only by a strong phonon absorption at 5.3 THz [25]. Apart from the zinc-blende crystals described earlier, GaSe is a promising semiconductor crystal that has been exploited recently for terahertz generation with an extremely large bandwidth of up to 100 THz [26,27].

1.2.2 Photoconductive antenna

Terahertz wave generation from photoconductive antenna is the earliest approach to generate single cycle terahertz waves. When a biased semiconductor substrate is excited with femtosecond laser pulses with photon energy greater than the bandgap, electrons and holes are produced under the illumination in conduction and valence bands, respectively. The applied DC biased field then will induce a rapid change of the density of photo-carriers and the corresponding transient current will eventually produce electromagnetic radiation in the far-field. However, the lifetime of the produced ultrashort current, which determines the bandwidth of radiated terahertz field, strongly depends on the carrier's lifetime of the semiconductor.

In 1975, Auston reported using silicon transmission line

structures as an photoconductive switch operating at a few picosecond range [28]. Mourou et. al. used a subpicosecond laser to trigger a GaAs photoconductive switch and observed a produced microwave transient of less than 3 ps [29]. Later, Grischkowsky et al. introduced particular antenna geometry and further improved the efficiency and the bandwidth of photoconductive antenna [30,31]. At present, low-temperature-grown GaAs (LT-GaAs) is the most popular material used for photoconductive antennas due to its short carrier lifetime. Shen et al. reported a ultra-broadband terahertz radiation with frequency components covering over 30 THz using a LT-GaAs photoconductive antenna [32].

1.2.3 Gas plasma

When focusing an intense laser beam into gases, the electrons will be released from their bounded atoms or molecules under the intense optical field. The formed mixture of electrons, ions, as well as the neutral atoms is known as plasma. Optical-ionized plasma can provide a broadband range of radiation, including extreme ultraviolet (XUV) [33], terahertz [34], and even radio frequency [35] and thus becomes a frontier research area. In early 1990s, Hamster et al. first demonstrated sub-pico second radiation by focusing mJ intense laser to ionize ambient air [34]. At that time, due to limitation of high power laser sources, the research is not generally applied until Cook and Hochstrasser further improved the generation efficiency by mixing fundamental beam and its second harmonic beam to excite the plasma [36].

One of the unique features of gas-plasma based terahertz sources is broad bandwidth. The bandwidth of such kind of terahertz wave sources is only determined by the exciting pulse duration. The reported detectable bandwidth is up to 100 THz [37], providing a useful tabletop broadband terahertz spectrometer.

1.3 Detection of broadband terahertz waves

In the development of THz-TDS, the requirement of detector has become a major issue. In terahertz time domain system, the time resolved detection is achieved by splitting laser pulses into pump pulses to excite pulsed terahertz radiation and optical sampling pulses to temporally probe terahertz pulses. By varying the relative time delay between pump pulses and probe pulses, the temporal terahertz field information can be obtained. However, for pulsed terahertz sources, a coherent detection scheme is required. Coherent detection means both the amplitude and phase information of the terahertz field can be obtained simultaneously. In this section, we will overview the most commonly used solid-state detection scheme and compare them with gas phase terahertz detectors.

1.3.1 Electro-optic crystals

Electro-optic detection [38–40] is the most common detection method used in the terahertz community. It is realized through an optical rectification process inside an electro-optic crystal, such as ZnTe or GaP. When the terahertz beam interacts with an optical sampling beam inside the crystal, the terahertz field will induce a birefringence in the crystal, which will result in a polarization rotation of the optical beam. Typically, a balanced detection scheme is used in this detection method to achieve better signal-to-noise ratio.

ZnTe and GaP are the most common crystals used in terahertz time-domain systems. Two principle factors of choosing a solid-state detector are the phonon absorption and phase match. It is hard for ZnTe and GaP to achieve very broad bandwidth is because that ZnTe and GaP have a phonon frequency at 5.3 [41] and 10.98 THz [42]. However, if a thin crystal is used to reduce absorption and to satisfy a better phase matching condition, broad bandwidth detection has been reported. Recently, GaSe crystal has been demonstrated to measure over 100 THz using a 10-fs-laser [27]. However, there are still some absorption dips in their spectrum.

1.3.2 Photoconductive antenna

Photoconductive antenna is the earliest pulsed terahertz wave detector [28]. It detects the terahertz radiation based on a transient photocurrent generated by ultrafast laser pulses. Typically, a photoconductive antenna contains a pair of micro-fabricated metal electrodes on a semiconductor substrate with a small gap between these two electrodes. When using a photoconductive antenna as the terahertz wave detector, a current meter is used to connect both electrodes. The terahertz field can induce a transient current between two electrodes when the photocarrier has been excited using a femtosecond laser pulses. By controlling the time delay between terahertz pulses and optical excitation pulses, the terahertz field information can be obtained.

Performance of a photoconductive antenna depends mainly on the following factors: the substrate material, the geometry of the antenna, and the excitation laser pulses. Especially, the detection bandwidth is essentially limited by the carrier lifetime. Materials with a short carrier lifetime, such as LT-GaAs or doped silicon, are usually selected as the substrate in order to increase the response speed of the photoconductive antenna. The typical lifetime of LT-GaAs is around 0.6 ps [43,44]. Shen et al. obtained terahertz radiation with frequency components over 30 THz using a backward collection scheme with LT-GaAs [32]. Kono et al. demonstrated an ultra-broadband detection of terahertz radiation up to 60 THz with a LT-

GaAs photoconductive antenna gated with 15 fs laser pulses [45].

1.3.3 Terahertz enhanced fluorescence or acoustics

In addition to solids, liquids and gases, the plasma state is often called the fourth state of matter. Different from other states, in plasma, charged particles such as electrons or ions are no longer bound together as atoms, molecules, showing unique responses under electromagnetic fields. Recently, Liu and Zhang had reported the electron kinetics in femtosecond laser-induced air plasma under terahertz illumination can result in an enhancement of fluorescence [46,47]. Especially, by obtaining a time-resolved terahertz radiation-enhanced emission of fluorescence, the temporal waveform of the terahertz field could be retrieved from the transient enhanced fluorescence, making omni-directional, and coherent detection available for THz-TDS. Furthermore, by using dual-color laser excitation to manipulate free electron drift, the coherent terahertz detection can be directly achieved [48]. Similarly, Clough et al. demonstrated that the acoustic waves from plasma also can be influenced by strong terahertz waves [49,50]. Thus, the coherent terahertz waves can be retrieved simply by "seeing" the fluorescence or "hearing" the acoustics of the plasma.

1.3.4 Gases

Compared with solid-state sensors, gaseous sensors for terahertz waves have been demonstrated to have great potential to further develop broadband THz-TDS. First, without phonon resonance, many gases do not possess absorption in the terahertz frequency, which can be used as broadband sensors. Second, gases are less dispersive, the phase match in a broad bandwidth is easy to achieve. Third, an infinitely high spectrum resolution can be achieved without Fabry-Parot effect introduced by reflective surface. Last but not the least, there is no damage limit for gaseous sensors and even if the laser intensity is high enough to ionize the gas, it can recover in nanosecond time scale.

Due to the increasing attention in air plasma-based terahertz source, a rising demand in broadband detection makes gases an ideal sensor for broadband terahertz waves. Initially, the quasi-coherent terahertz wave detection in ambient air was first reported through a four wave mixing process [51]. Later, by introducing a bias field induced second harmonic as the heterodyne local oscillator, the detection is confined in coherent region without a high probe power requirement [52]. With the development of terahertz gas photonics, broadband terahertz wave's detection with gases demonstrates its unique potential in THz-TDS.

2 Terahertz wave detection with gases

The intense terahertz waves generated from laser-induced plasma in gaseous media present promising capabilities for sensing and imaging techniques. However, simultaneously coherent and broadband detection remains challenging. Previous works with electro-optics crystals and photoconductive antenna detectors have been reported to reach frequencies up to 100 THz [27,45], but there are gaps in their spectra due to phonon resonances. Unlike solid-state sensors, gaseous media have no phonon resonances, exhibit much lower dispersion, and are continuously renewable.

Terahertz wave detection with gases is governed by a third order nonlinear process: generating second harmonic photons when mixing one terahertz photon and two fundamental photons together. In the 1990s, terahertz field-induced second harmonic generation (TFISH) was initially observed in solids [53] and liquids [54]. Terahertz wave detection from TFISH was initially demonstrated in silicon by Nahata and Heinz in 1998 using surface nonlinear susceptibility [53]. Dai et al. first demonstrated quasi-coherent terahertz wave detection through gaseous media via TFISH in laser-induced air plasma with ultrashort laser pulses [51]. However, a strong plasma background as local oscillator is required to achieve semi-coherent detection. Recently, heterodyne terahertz wave detection has been demonstrated to improve the detection in the coherent region by introducing a bias field-induced second harmonic as local oscillator [52]. In this method, a modulated DC bias is placed on the focus spot to provide a local bias-induced second harmonic oscillator. Owing to the modulation of the bias-induced second harmonic, the lock-in amplifier can directly isolate the signal proportional to the terahertz field. Directly coherent and broadband detection is achieved.

In this section, we systematically studied air-biased coherent detection using various gases [55–57]. First of all, we systematically investigated optimization of air-biased coherent detection with different probe pulse energy, bias field strength, and gas nonlinear susceptibility under a plane wave assumption. Then, by considering a focused Gaussian beam, we investigated the phase match, focus condition and Gouy phase shift to further improve the efficiency of air-biased coherent detection. Finally, we performed a series of measurements with various pulse durations to confirm the relationship between detection bandwidth and pulse duration.

2.1 Theoretical background

Terahertz wave detection with gases is achieved through a third order nonlinear frequency mixing process. By combining one terahertz photon with two fundamental

photons, a second harmonic photon is produced through a four-wave mixing process. Analytical knowledge of this four-wave mixing process will provide the guidance to optimize air-biased-coherent-detection (ABCD) system. In the following context, we will discuss this terahertz detection process first under plane wave approximation and then consider it under a focused Gaussian beam condition.

2.1.1 Plane wave approximation

Considering terahertz wave detection under the plane wave approximation is the simplest case. Since the terahertz wave detection using a gaseous medium is accomplished through a four-wave mixing process: producing second harmonic photons when mixing one terahertz photon and two fundamental photons together. The emitted second harmonic field can be expressed as

$$E_{2\omega}^{\mathrm{THz}} \propto \chi^{(3)} E_{\omega} E_{\omega} E_{\mathrm{THz}}, \tag{1}$$

where $\chi^{(3)}$ is the relevant component of the third order nonlinear susceptibility tensor of the gas and E_{ω}, $E_{2\omega}$, and E_{THz} are the electrical field vectors of fundamental, second harmonic and terahertz beams, respectively. Due to the response characteristic of our detector, the measured quantity is proportional to intensity, which is

$$I_{2\omega}^{\mathrm{THz}} \propto [\chi^{(3)} I_{\omega}]^2 I_{\mathrm{THz}}. \tag{2}$$

In this expression, the detected second harmonic intensity is proportional to the intensity of the terahertz field, which turns out to be incoherent detection. Initially, quasi-coherent terahertz detection through gaseous media was achieved via terahertz field-induced second-harmonic generation in laser-induced air plasma with ultrashort laser pulses. By the presence of plasma, the nonlinear process inside plasma provides a background second harmonic signal $E_{2\omega}^{\mathrm{LO}}$, which acts as a local oscillator. Thus, the detected second harmonic intensity became the interference of these second harmonic photons,

$$\begin{aligned} I_{2\omega} &\propto (E_{2\omega}^{\mathrm{THz}} + E_{2\omega}^{\mathrm{LO}})^2 \\ &\propto (E_{2\omega}^{\mathrm{THz}})^2 + (E_{2\omega}^{\mathrm{LO}})^2 + 2\chi^{(3)} I_{\omega} E_{2\omega}^{\mathrm{LO}} E_{\mathrm{THz}}. \end{aligned} \tag{3}$$

If the background signal $E_{2\omega}^{\mathrm{LO}}$ is sufficiently strong, Eq. (3) can be simplified to

$$I_{2\omega} \propto (E_{2\omega}^{\mathrm{LO}})^2 + 2\chi^{(3)} I_{\omega} E_{2\omega}^{\mathrm{LO}} E_{\mathrm{THz}},$$

which shows that the detected second harmonic is associated with E_{THz}, resulting in quasi-coherent detection of the terahertz waves. However, in this quasi-coherent detection, due to the existence of background signal $(E_{2\omega}^{\mathrm{LO}})^2$, the waveform is distorted and signal to noise ratio is limited.

Introducing a similar concept, heterodyne terahertz wave detection has been demonstrated to improve the detection in the coherent region by introducing a modulated local bias-induced second harmonic as local oscillator. Analogous to terahertz field-induced second harmonic, a second harmonic signal can be introduced by applying a DC bias field, which can be expressed as

$$E_{2\omega}^{\mathrm{DC}} \propto \chi^{(3)} E_{\omega} E_{\omega} E_{\mathrm{DC}}, \tag{4}$$

where E_{DC} is the electrical field amplitude of the bias field. Then, the detected second harmonic intensity became

$$\begin{aligned} I_{2\omega} &\propto (E_{2\omega}^{\mathrm{THz}} \pm E_{2\omega}^{\mathrm{DC}})^2 \\ &\propto (E_{2\omega}^{\mathrm{THz}})^2 + (E_{2\omega}^{\mathrm{DC}})^2 \pm 2\left(\chi^{(3)} I_{\omega}\right)^2 E_{\mathrm{DC}} E_{\mathrm{THz}}. \end{aligned} \tag{5}$$

In Eq. (5), we still have the offset terms $(E_{2\omega}^{\mathrm{THz}})^2 + (E_{2\omega}^{\mathrm{DC}})^2$. However, by modulating the DC field at certain frequency and referring the lock-in amplifier to this modulation frequency, the cross term can be isolated from all DC background. Here, to simplify the process, we modulated the DC bias field at half of laser repetition rate, which is 500 Hz. In this case, the offset terms $(E_{2\omega}^{\mathrm{THz}})^2$, and $(E_{2\omega}^{\mathrm{DC}})^2$ are operating at l kHz laser repetition rate. Only the cross term $2\left(\chi^{(3)} I_{\omega}\right)^2 E_{\mathrm{DC}} E_{\mathrm{THz}}$, which is directly proportional to the field strength of terahertz waves, are operating at 500 Hz. The measured second harmonic intensity can be expressed as

$$I_{2\omega} \propto [\chi^{(3)} I_{\omega}]^2 E_{\mathrm{DC}} E_{\mathrm{THz}}, \tag{6}$$

which is pure coherent detection of terahertz waves.

Equation (6) exhibits the general description of the detected second harmonic intensity under plane wave assumption without considering phase matching condition. The equation directly shows that the detected second harmonic intensity is related to nonlinearity of gases, probe pulse energy, electrical field strength of bias field and terahertz field. In the following content, a series of experiments were performed to test the validity of Eq. (6).

2.1.2 Gaussian beam consideration

In last a few sections, we only consider four-wave mixing process under plane wave approximation in which case all of the interacted waves are taken to be infinite plane waves. However, in practice, the laser beams have an approximately Gaussian profile and are focused into gas media to achieve high intensity. Thus, in this section, we take the focused Gaussian beam into account and simulate this field-induced second harmonic generation process [58,59].

If both the incident fundamental beam and terahertz wave have a Gaussian field intensity distribution, which

can be expressed as

$$E_\omega(r,z) = \frac{E_\omega}{1+\mathrm{i}z/z_\mathrm{R}}\mathrm{e}^{-r^2/w_0^2(1+\mathrm{i}z/z_\mathrm{R})}, \quad (7)$$

$$E_\mathrm{THz}(r,z) = \frac{E_\mathrm{THz}}{1+\mathrm{i}z/z_\mathrm{T}}, \quad (8)$$

where E_ω and E_THz are the amplitudes of fundamental beam and terahertz beam, respectively, and w_0 is the beam waist. Here, z_R and z_T are the Rayleigh length of the fundamental and terahertz beams, respectively. Since the terahertz beam waist (in mm) is much larger than that of optical beam (in μm), the radial variation of terahertz field is neglected here. Similarly, the trial solution for the second harmonic wave can be expressed as

$$E_{2\omega}(r,z) = \frac{E_{2\omega}(z)}{1+\mathrm{i}z/z_\mathrm{R}}\mathrm{e}^{-2r^2/w_0^2(1+\mathrm{i}z/z_\mathrm{R})}. \quad (9)$$

Consider the paraxial wave equation to describe second harmonic generation process, which is

$$2ik_{2\omega}\frac{\partial E_{2\omega}}{\partial z} + \nabla_\mathrm{T}^2 E_{2\omega} = -\frac{16\pi\omega^2}{c^2}\chi^{(2)}E_\omega^2\mathrm{e}^{-\mathrm{i}\Delta kz}. \quad (10)$$

Here, $\Delta k = 2k_\omega - k_{2\omega}$ is the wave vector mismatch. Since gas is a centro-symmetric medium, the static second order nonlinear susceptibility $\chi^{(2)}$ is zero. Thus, for field-induced second harmonic generation, $\chi_\mathrm{eff}^{(2)}$ is actually a function of field, which can be expressed as

$$\chi_\mathrm{eff}^{(2)} = \chi^{(3)}E_\mathrm{THz}^* + c.c.. \quad (11)$$

Note that we have taken the conjugate of terahertz field here. Due to the Gouy phase shift, which is the phase shift of π radians that a Gaussian beam of light experiences in passing through its focus, the resulted polarization of the second harmonic will experience a summation of phase shift from all incident waves. Consequently, in the two possible processes, the $\omega+\omega-\Omega_\mathrm{THz}$ process will couple more efficiently to the generated second harmonic than $\omega+\omega+\Omega_\mathrm{THz}$ [60]. Here, we neglect the latter process all together.

Letting Eqs. (7), (8) and (9) be the trial solution to Eq. (10), we find

$$E_{2\omega}(z) = \frac{\mathrm{i}4\pi\omega}{nc}\chi^{(3)}E_\omega^2E_\mathrm{THz}^*J(\Delta k,z_0,z), \quad (12)$$

where n is the index of refraction at fundamental wavelength. The integral $J(\Delta k,z_0,z) = \int_{-\infty}^{+\infty}\exp(\mathrm{i}\Delta kz')/[(1+\mathrm{i}z'/z_\mathrm{R})(1-\mathrm{i}z'/z_\mathrm{T})]\mathrm{d}z'$ can be evaluated by contour integration. Thus,

$$E_{2\omega}^\mathrm{THz} = \frac{\mathrm{i}8\pi^2\omega}{nc}\chi^{(3)}E_\omega^2E_\mathrm{THz}\frac{z_\mathrm{R}z_\mathrm{T}}{z_\mathrm{R}+z_\mathrm{T}}\mathrm{e}^{z_\mathrm{T}\Delta k} \quad (13)$$

with the assumption $\Delta k<0$.

Next, we consider DC-induced second harmonic in the same way. The electrodes used in our experiments are cylindrical wire. The electric field distribution can be presented as [61]

$$E_\mathrm{DC}(z) = \frac{2V}{d\,\mathrm{arcosh}(l/2a)}\frac{1}{1+(2z/d)^2}, \quad (14)$$

where V is the applied voltage, l is the separation between the electrodes, a is the radius of wire, and $d^2 = l^2-4a^2$.

A similar treatment can be made for the DC field-induced second harmonic, substituting Eq. (14) into Eq. (10), the solution is

$$E_{2\omega}^\mathrm{DC} = \frac{\mathrm{i}8\pi^2\omega}{nc\,\mathrm{arcosh}(l/2a)}\chi^{(3)}E_\omega^2V\frac{z_\mathrm{R}}{2z_\mathrm{R}+d}\mathrm{e}^{d\Delta k/2}. \quad (15)$$

In heterodyne detection, the detected second harmonic is the cross term of the terahertz-induced second harmonic and bias field-induced second harmonic, which can be expressed as

$$I_{2\omega} \propto E_{2\omega}^\mathrm{DC}E_{2\omega}^\mathrm{THz} \propto \left(\chi^{(3)}I_\omega\right)^2E_\mathrm{THz}V\frac{z_\mathrm{R}^2z_\mathrm{T}}{(z_\mathrm{R}+z_\mathrm{T})(2z_\mathrm{R}+d)}\mathrm{e}^{(z_\mathrm{T}+d/2)\Delta k}, \quad (16)$$

where the simplification $n = 1$ has been made.

From Eq. (16), the detected second harmonic is not only dependent on the third order nonlinear susceptibility $\chi^{(3)}$, probe beam energy I_ω, terahertz field strength E_THz and electrical field strength V, but also the Rayleigh lengths of the terahertz beam and optical beam, as well as phase matching.

Let us first consider the phase matching of this process. For a co-propagating geometry, the phase mismatch is from dispersion between the fundamental beam and second harmonic beam. Since the index of refraction varies linearly with pressure, the phase mismatch Δk is also dependent on pressure. Thus, the phase mismatch can be expressed as

$$\Delta k = -p*dk = -2\pi p\frac{\Delta n_0}{\lambda_{2\omega}}, \quad (17)$$

where $dk = 2k_\omega - k_{2\omega} = \frac{4\pi n_\omega}{\lambda_\omega} - \frac{2\pi n_{2\omega}}{\lambda_{2\omega}} = 2\pi\frac{\Delta n_0}{\lambda_{2\omega}}$ is the phase mismatch at one atmosphere of pressure, p is the pressure in atmospheres, $\Delta n_0 = n_{2\omega}-n_\omega$ is the dispersion in one atmosphere and $\lambda_{2\omega}$ is the wavelength of the second harmonic.

Since $\chi^{(3)}$ is also linearly dependent on pressure, it can be expressed as $\chi^{(3)} = \chi_0^{(3)}p$, where $\chi_0^{(3)}$ is the third order nonlinear susceptibility at one atmosphere.

The detected second harmonic intensity could be written as

$$I_{2\omega} = A\frac{z_{\mathrm{R}}^2 z_{\mathrm{T}}}{(z_{\mathrm{R}}+z_{\mathrm{T}})(2z_{\mathrm{R}}+d)}\left(\chi_0^{(3)}p\right)^2 \mathrm{e}^{-(z_{\mathrm{T}}+d/2)dkp}, \quad (18)$$

where $A = (\mathrm{i}8\pi^2\omega c^{-1}I_\omega)^2 E_{\mathrm{THz}}V$ contains the fixed parameter under a certain experimental condition.

From Eq. (18), the optimal pressure of a certain gas for terahertz detection can be derived:

$$p_{\mathrm{opt}} = \frac{2}{(z_{\mathrm{T}}+d/2)dk}. \quad (19)$$

According to Eq. (19), the optimal pressure for a certain gas sensor is related to the Rayleigh length of the terahertz beam, the geometry of the electrodes and optical dispersion. Moreover, the Rayleigh length of the optical beam has no effect on the optimal pressure.

Therefore, the maximum signal at optimal pressure is

$$I_{2\omega} = \frac{A}{e^2}\frac{4z_{\mathrm{R}}^2 z_{\mathrm{T}}}{(z_{\mathrm{R}}+z_{\mathrm{T}})(2z_{\mathrm{R}}+d)(z_{\mathrm{T}}+d/2)^2}\left(\frac{\chi_0^{(3)}}{dk}\right)^2. \quad (20)$$

According to Eq. (20), all of the terms related to the gas are confined to the ratio of $\chi_0^{(3)}$ to dk, and so it is possible to introduce a figure of merit (FOM) of the nonlinear gaseous media:

$$\mathrm{FOM} = \left(\frac{\chi_0^{(3)}}{dk}\right)^2. \quad (21)$$

Equation (21) points out the most essential parameters to characterize the sensitivity of terahertz wave gaseous sensors.

2.2 Experimental details

To test the validity of above analytical models, we performed a systematic study using various gases. Figure 1 shows the schematic of the experimental setup. The experiment was performed with a Spectra-Physics Hurricane amplified laser system, which delivers 800 nm, 80 fs, 650 μJ pulses at a 1 kHz repetition rate. The laser pulses were split into pump and probe beams by a 80%–20% beam splitter. The optical pump beam was focused with a lens with 100 mm focal length through a 100 μm thick type-I beta barium borate (BBO) crystal to generate the second-harmonic pulses. Both fundamental pulses and second-harmonic pulses were focused into air to produce a terahertz pulse by ionizing air at the focus. The radiated terahertz wave was collected by a 90° off-axis parabolic mirror and focused again by another parabolic mirror. The optical probe beam was sent through a time delay stage and then focused by a 200 mm lens through a hole in the second parabolic mirror. Thus, the terahertz wave propagated collinearly with the optical probe beam and was focused into a gas cell at the same location. The induced second harmonic signal was collected by a UV lens, passed through a pair of 400 nm bandpass filters and detected by a PMT.

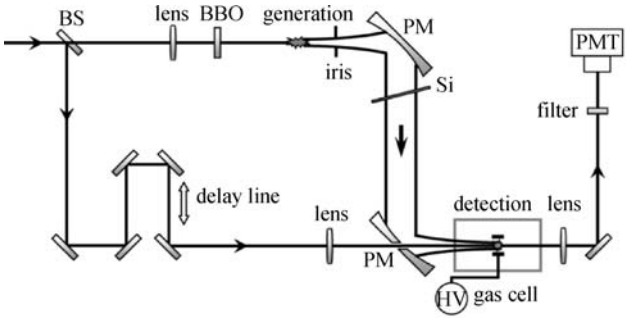

Fig. 1 Schematic of experimental setup. BS: beam splitter. BBO: type-I beta barium borate. PM: parabolic mirror. PMT: photomultiplier tube. HV: high voltage modulator. Terahertz wave was generated through laser-induced plasma in air. An iris with a diameter of 10 mm was placed at a distance about 50 mm after the plasma. A high-resistivity silicon wafer was used to block the residual pump beam. The terahertz beam and probe beam were focused collinearly in the presence of a modulated bias, resulting in a second harmonic signal, which was detected by PMT

Figure 2 shows the illustration of the gas cell used in our experiment. The cell body was made of stainless steel. The entrance and exit windows were made, respectively, of 2 mm and 3 mm thick fused quartz with 25 mm diameter. Other materials can be used as the entrance window, such as polymethylpentene (TPX) and silicon, but they all require a special design of the cell. Here, we were not concerned with loss of high frequency components and therefore used quartz as the entrance window for simplicity. The longitudinal length of the cell was 50 mm. The bottom of the cell was connected to a gas distribution system, which can pump the cell to vacuum (below 20 mtorr) or introduce a certain amount of each gas into the cell. The pressure inside can be precisely monitored with a piezoelectric pressure gauge. A pair of thin electrodes with a 1 mm gap were placed at the focal spot through an electrical feed-through connected to a high voltage modulator which was synchronized with the laser, providing tunable voltage up to 3.2 kV at a frequency of 500 Hz.

2.3 Results and discussion

2.3.1 Probe pulse energy

From Eq. (6), the detected second harmonic intensity is quadratically dependent on probe pulse energy, which makes probe power the first parameter to be considered.

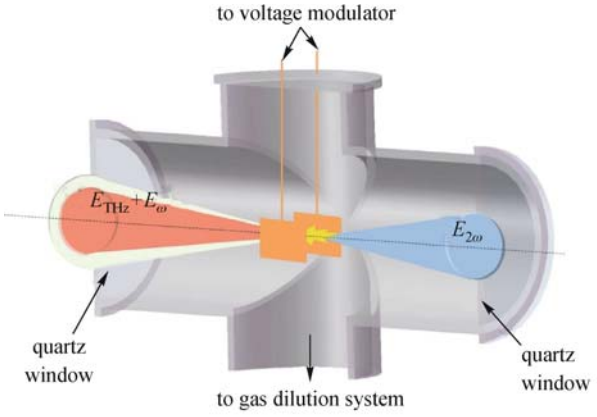

Fig. 2 Schematic illustration of gas cell. Both the entrance and exit windows were made of quartz, which is relatively transparent to both fundamental and second harmonic beams. The quartz material has low absorption at the frequency below 5 THz. The electrical field was connected through an electrical feed-through at the top of gas cell and the gases were introduced through the bottom of the cell

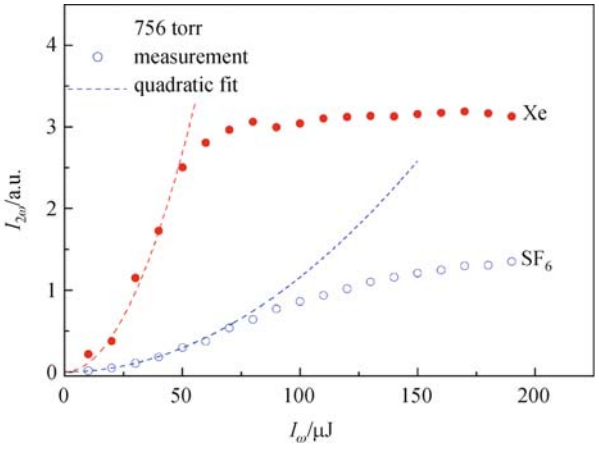

Fig. 3 Measured second harmonic intensity ($I_{2\omega}$) versus the probe pulse energy (I_{ω}) at a bias field of 7.5 kV/cm, and gas pressure of 756 torr with Xe and SF_6 gases. Dots are from measurements and dashed lines are quadratic fits. The deviation of the probe energy dependence above 50 μJ for Xe and 70 μJ for SF_6 are consistent with the onset of intensity clamping due to plasma formation

Figure 3 depicts the relation of the second harmonic signal intensity on the probe pulse energy for Xe and SF_6, which was measured by adjusting a neutral density filter in the probe beam. Based on the trend seen in Fig. 3, we can separate the detected signal into two regions: (a) low pulse energy and (b) high pulse energy. At the low pulse energy region, the measured second harmonic signal evolves quadratically with respect to probe pulse energy, as is expected from Eq. (6). However, this behavior is modified at higher probe pulse energy region because of intensity clamping [62], which occurs during and after plasma formation. Furthermore, after plasma formation, the fluorescent background will limit the signal-to-noise ratio and dense plasma will also introduce absorption in terahertz range and distort detected terahertz waveform, which we will discuss in Section 2.3.2. In this heterodyne detection, there is no minimum requirement for probe pulse energy, which confirms that four-wave mixing is the principle mechanism responsible for this process.

2.3.2 Plasma absorption

As we discussed in Section 2.3.1, after the plasma is created, the intensity clamping effect will limit the peak power of laser pulses and induce a saturation effect on detection efficiency. Moreover, we have noticed that the plasma also exhibits absorption at certain frequency range. Especially, when performing ABCD with short pulses, this effect becomes significant due to the increasing of plasma density.

We performed an extra experiment with Coherent Legend Elite DUO amplifier, which can deliver 35 fs, 800 nm pulses with up to 6 mJ pulse energy. A probe beam with up to 200 μJ pulse energy was used as temporal probe for the terahertz wave. A pair of electrodes was positioned around the center of the plasma. In this case, the measured terahertz waveforms will reflect the absorption effect from the plasma. A probe power dependence measurement was performed in an identical approach. Figure 4 shows a series of measured waveforms and corresponding spectra at various probe pulse energy. We observed that the measured waveforms experienced a significant shape change after the plasma was created. Interestingly, the absorption frequency, which was shown by black arrows on the corresponding spectrum, showed a red shift while increasing the probe pulse energy.

It is possible that the plasma exhibits a resonance frequency at terahertz frequency range. However, the plasma frequency usually shifts toward high frequency while increasing plasma density. Therefore, the mechanism of this phenomenon is still unclear at this moment and further systematic study is required. The scattering effect and waveguide effect of the plasma column are the two possible mechanisms.

2.3.3 Bias field strength

Due to the constraint of probe pulse energy resulting from intensity clamping, increasing bias field strength is another approach to improve the second harmonic intensity. Figure 5 depicts the detected signal as a function of the bias field strength using Xe, SF_6 and air as the sensing media, together with linear fits (dashed lines). To reduce the sophisticated effects associated with high pressure, tests were performed at a pressure of 100 torr (Fig. 5(a)), in

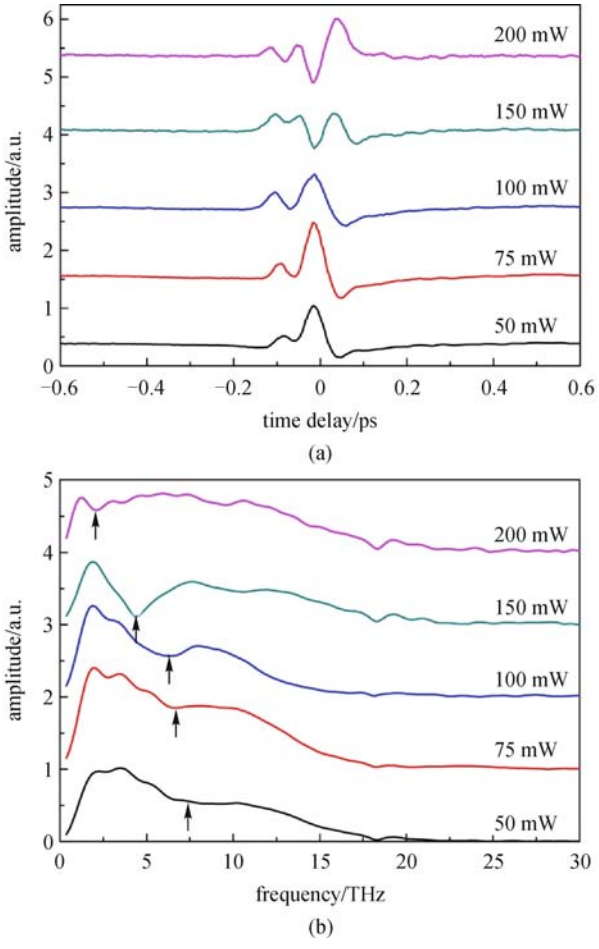

Fig. 4 Terahertz (a) waveforms and (b) spectra obtained with different probe pulse energy. Electrodes were placed around the center of plasma. Black arrows are the guides for the absorption frequency, which shows a red shift while increasing the probe pulse energy

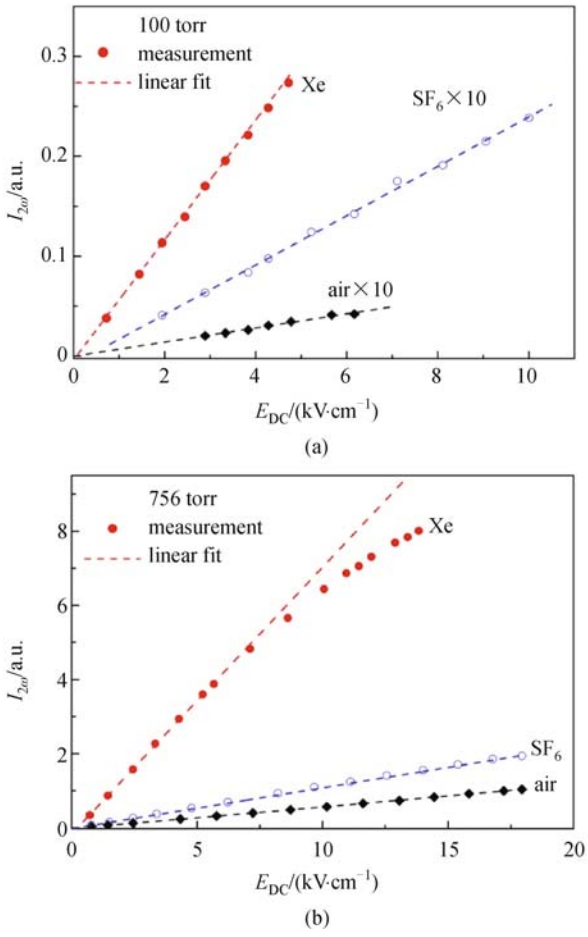

Fig. 5 Measured second harmonic intensity ($I_{2\omega}$) versus DC bias field (E_{DC}) at gas pressure of (a) 100 torr and (b) 756 torr, with a probe pulse energy of 50 μJ. Dots are from measurements and dashed lines are linear fits

which the detected second harmonic from Xe exhibited two orders enhancement over that from nitrogen. In additional tests performed at one atmosphere (Fig. 5(b)), under the same conditions, the detected terahertz signal from Xe exhibits one order higher intensity than that from air.

2.3.4 Nonlinearity of gases

From the above discussion, one of the efficient approaches to enhancing detected second harmonic intensity is selecting gases with high nonlinearities as sensors. We performed a series of measurements with various gas samples. The gaseous samples selected here are nitrogen (N_2), xenon (Xe), sulfur hexafluoride (SF_6), carbon disulfide (CS_2), cyclopentene (C_5H_8) and alkane gases (CH_4, C_2H_6, C_3H_8, n-C_4H_{10}, n-C_5H_{12} and C_6H_{14}). Most of the gases chosen here have relatively large third order nonlinear susceptibilities and lower absorption in the terahertz range due to their symmetric structures. Some samples, such as CS_2, C_5H_8, C_5H_{12} and C_6H_{14}, are in liquid phase under room temperature. To obtain pure sample vapor, the sample container is frozen with liquid nitrogen and pumped to below 20 mTorr to achieve air-free condition. After the sample is melted and warmed to room temperature, sample vapor can be introduced into the gas cell and the pressure inside is precisely controlled with the gas dilution system. The saturated vapor pressure at room temperature for CS_2, C_5H_8, C_5H_{12} and C_6H_{14} are about 301, 316, 428 and 132 torr, respectively.

The detected second harmonic signal as a function of normalized third order nonlinear susceptibility $\chi^{(3)}$ are shown in Fig. 6. The dashed line is the quadratic fit according to Eq. (6). To reduce phase mismatch, intensity clamping and electrical breakdown effects for all the gases, the measurements were performed at a pressure of 100 torr, probe pulse energy of 20 μJ and a bias field of 5 kV/cm. Furthermore, we neglected the ionization effect on $\chi^{(3)}$ since the probe pulse energy used here is much lower than

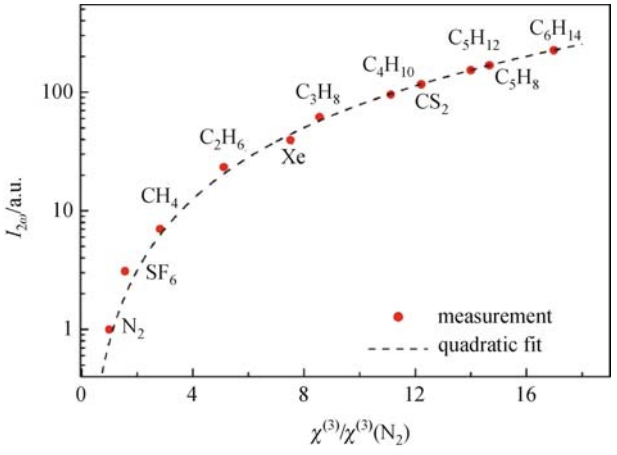

Fig. 6 Detected second harmonic intensity ($I_{2\omega}$) verses third order nonlinear susceptibility ($\chi^{(3)}$) of gases. Red dots are experimental data and black dashed line is the quadratic fit. *Y*-axis is normalized with the reference signal taken with 100 torr nitrogen gas at the same experimental condition. Also, all the $\chi^{(3)}$ are normalized with that of nitrogen

the ionization threshold. The data of detected second harmonic intensity were processed by integrating the detected terahertz wave spectra from 0.3 to 10 THz. The values of $\chi^{(3)}$ are estimated from Ref. [63]. Values of $\chi^{(3)}$ for CS_2, C_5H_8, C_5H_{12} and C_6H_{14} are from our direct measurements of DC bias-inducted second harmonic by blocking the terahertz beam.

We have noticed that most of alkane gases present relatively high $\chi^{(3)}$. The high order nonlinear susceptibility is used to describe the distorted response of molecules under strong electrical field. Based on Boyd's discussion [64], the third order polarizability of molecule γ depends on L^{10}, where L is the size of a molecule [65]. Note that nonlinear coefficients increase significantly with the size of a molecule. Especially for the alkane gas family, the polarizability γ has a fairly linear dependence with the number of carbon atoms in the molecules [66]. Hexane vapor exhibits a nearly 240 times improvement in second harmonic intensity compared to nitrogen.

One type of hydrocarbon, which contains alternating single and double bonds, is called a conjugated hydrocarbon. These molecules can possess an extremely large nonlinear optical response because the π bond is very sensitive to the external electrical field [66]. The π electrons tend to be delocalized and more loosely bound and, therefore, respond more freely to an applied optical field. In Fig. 6, we also present the measured result from cyclopentene, which is a kind of cycloalkene containing one double bond. As expected, C_5H_8 produces more second harmonic than C_5H_{12}.

Another important aspect is that, although the polarizability γ increases with the increase of molecule size, samples with large size molecule tend to be in the liquid phase under room temperature. Since $\chi^{(3)}$ is not only associated with γ but also molecular density, mixing various nonreactive gases with high third order polarizability together is one approach to increase the molecular density. We have demonstrated that, with 300 torr C_5H_{12} and 400 torr C_3H_8, the detected second harmonic signal is about 1.5 times higher compared to only 700 torr C_3H_8 at the same experimental condition.

2.3.5 Phase matching

In nonlinear frequency mixing process, the phase matching condition is a very important factor to be considered. Especially in broadband detection, in order to satisfy phase match in a broader frequency range, a less dispersive media is required. In this section, we will discuss phase matching condition in terahertz wave detection process.

To verify the phase matching effect during the field-induced second harmonic generation process, pressure dependence measurements were performed with xenon, propane and *n*-butane, all of which present relatively large dispersion. By inserting an iris with 10 mm diameter after the plasma (Fig. 1), the Rayleigh length of the terahertz beam was controlled by confining the beam diameter.

Figure 7 shows pressure dependence of detected second harmonic intensity from xenon, propane and *n*-butane gas at various Rayleigh lengths of the terahertz beam along with fitting curves. The probe beam power is 20 mW and bias field strength is set at about 8 kV/cm to avoid breakdown at low pressure. The dashed lines are calculated fits from Eq. (18). In the calculation, the Rayleigh length of the optical beam is estimated to be 2.5 mm and the electric field parameters a and l are 250 μm and 1 mm, respectively. The dispersion relation of xenon is given in Ref. [67]. From the fitting curve, the Rayleigh lengths of the terahertz beam are estimated to be 0.8 mm without iris and 1.5 mm with iris. Considering the loss of terahertz wave intensity caused by inserting the iris, the two sets of data are all normalized with reference signals taken with 756 torr air at each condition respectively. As expected, the optimal pressure shifts toward high pressure while decreasing Rayleigh length of the terahertz beam. Identical phenomena were also observed with propane and *n*-butane. It should be pointed out that the theoretical fit for propane and *n*-butane data are based on estimated phase mismatch factor dk due to the inadequate information about their dispersion.

By mapping the detected terahertz spectra versus pressure (Fig. 8), a clear shift of the center frequency toward high frequencies is observed while increasing gas pressure. This is due to the frequency dependent phase match condition. The bandwidth is limited since the quartz window of the gas cell absorbs most of the frequency components above 5 THz. The same phenomenon was also observed with propane and n-butane gases. Noticed that

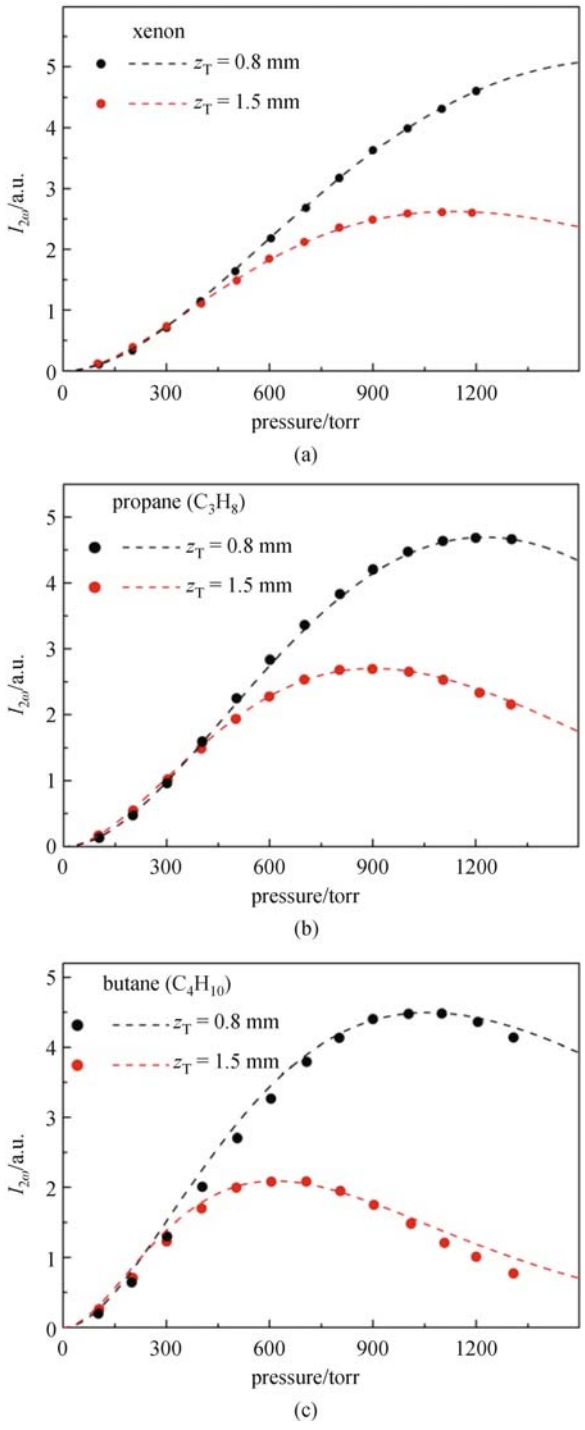

Fig. 7 Pressure dependence of detected second harmonic intensity from (a) xenon; (b) propane and (c) *n*-butane gas at different focus condition of terahertz beam. Optical probe beam power was set to be 20 mW and bias field strength is about 8 kV/cm. The Rayleigh length of terahertz beam was controlled by an iris in terahertz beam path. Black (red) dots are from measurements without iris (with iris) condition and dashed lines are fit from analytical expression. Fitted Rayleigh lengths are z_T = 0.8 mm and z_T = 1.5 mm, respectively

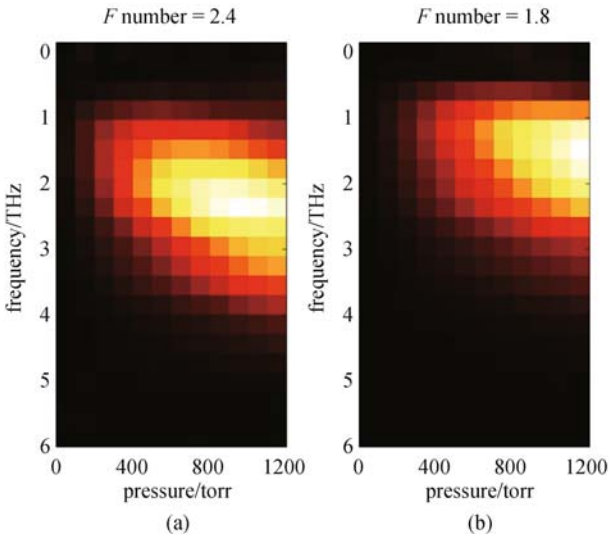

Fig. 8 2D plot of detected terahertz spectra with Xe versus pressure at different terahertz focus condition. The terahertz Rayleigh lengths without and with iris were estimated to be 0.8 and 1.5 mm, respectively. The different phase match of each frequency component results in a spectral shift toward high frequency. (a) *F* number = 2.4; (b) *F* number = 1.8

the phase mismatch factor $\exp[-(z_T + d/2)dkp]$ is actually frequency dependent since z_T and dk vary with frequency. Therefore, each frequency component of the terahertz beam experiences different phase matching conditions since higher frequency components are focused more tightly and exhibit longer Rayleigh lengths.

To investigate the frequency-dependent phase match, taking several frequency components, Fig. 9 plots the normalized amplitude of each frequency component versus pressure. Each frequency component is normalized with the maximum amplitude to make the peak clear. From Fig. 9, it is obvious that the peak shifts to high frequencies with high pressures.

2.3.6 Gouy phase shift

Gouy phase shift is a π phase shift process that every Gaussian pulse experiences during a focusing process [68,69]. It is named after a French scientist, L. G. Gouy, who discovered this phenomenon in 1890. It has been demonstrated that the Gouy phase shift should result in a polarity reversal of single-cycle terahertz pulses as they evolve through a focus, which enables direct, noninterferometric observations of the Gouy shift using terahertz time domain spectroscopy [70]. In this section, an experimental investigation of Gouy phase shift in ABCD are performed and discussed.

The Gouy phase of any Gaussian pulses can be written as

$$\phi_G = -a\tan\left(\frac{z}{z_R}\right), \tag{22}$$

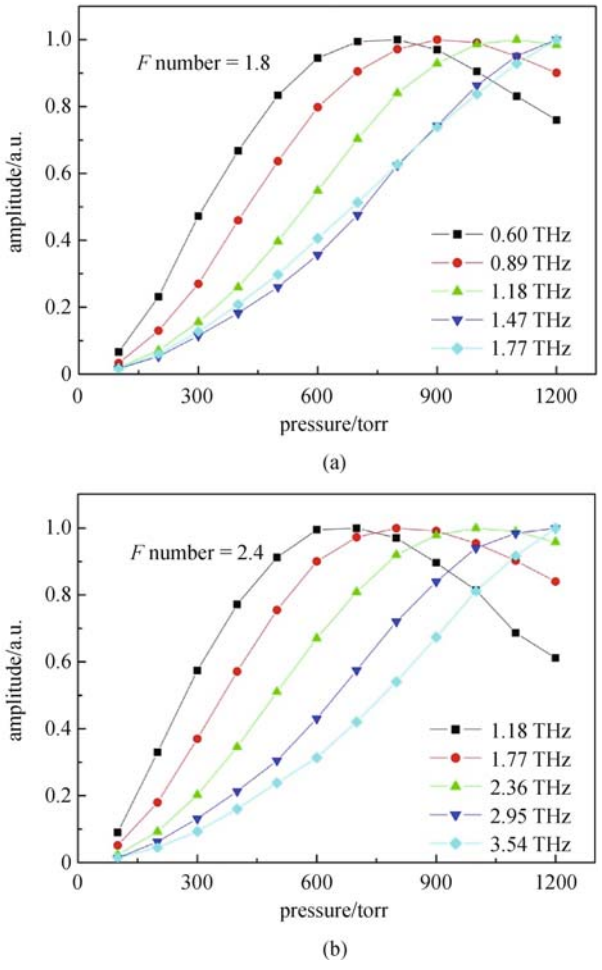

Fig. 9 Pressure dependence of various frequency components with Xe sensor at (a) F number = 1.8 and (b) F number = 2.4. The probe beam power is 20 mW and bias field strength is about 8 kV/cm. Data were normalized with peak value for clarity

where z is the propagating axis and z_R is the Rayleigh range.

Here, we consider a perfect aligned ABCD system, which means the focuses of optical beams and terahertz beams are exactly overlapped at the same position with each other (as shown in Fig. 10). In the ABCD process, the measured terahertz phase would be determined by the phase difference between the terahertz wave and the optical beam.

Considering the four-wave mixing process, which happens in ABCD, making the Gouy phase terms exclusive, the optical beam (E_ω) and terahertz (E_{THz}) beam can be written as

$$E_\omega(z) = E_\omega \frac{w_R^0}{w_R(z)} \exp\left(i\phi_R(z)\right), \tag{23}$$

$$E_{THz}(z) = E_{THz} \frac{w_T^0}{w_T(z)} \exp\left(i\phi_T(z)\right), \tag{24}$$

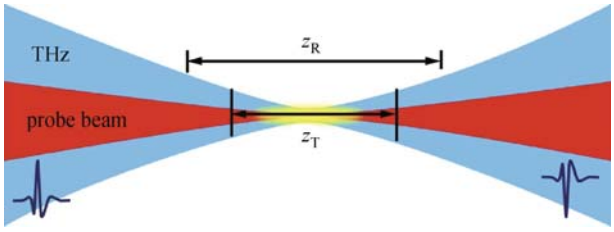

Fig. 10 Illustration of Gouy phase shift in an ABCD system. z_R and z_T are the Rayleigh range of optical probe beam and terahertz beam, respectively

where w_R^0 and w_T^0 are the beam waist of optical probe beam and terahertz beam, and ϕ_R and ϕ_T are the Gouy phase of optical probe beam and terahertz beam, respectively. $w_R(z) = w_R^0\sqrt{1+(z/z_R)^2}$ and $w_T(z) = w_T^0\sqrt{1+(z/z_T)^2}$ represent the 1/e radius of the field distribution. Here, we ignored the radial distribution of both beams. Thus, the measured second harmonic beam $I_{2\omega} \propto [E_\omega]^4 E_{DC} E_{THz}$ will experience the phase shift of $4\phi_R(z) \pm \phi_T(z)$. The "±" sign is corresponding to process $\omega + \omega \pm \Omega$. Figure 11 shows a calculated Gouy phase shift along the propagation direction (z-axis). The blue curves in Fig. 11 represent the actually measured phase of terahertz waves with ABCD. A clear phase reversal is predicted in our calculation.

We used a pair of thin electrodes to verify the Gouy phase shift effect in ABCD. The electrodes were made of copper wire with a diameter of 0.5 mm. The electrodes were mounted on a translating stage, which can move along propagation direction (z-axis). The measured terahertz waveforms and corresponding spectra are shown in Fig. 12. It is clear that the measured terahertz waveforms are shown a significant phase different along propagation direction. The corresponding spectra shows a broaden effect at the maximum value where the terahertz focus is. Since high frequency components exhibit relatively smaller Rayleigh range, the Gouy phase effect is more significant for these components.

Figure 13 shows the extracted phase from measured terahertz waveforms together with a theoretical fit. The Rayleigh ranges of optical probe beam and terahertz beam are estimated to be 1.5 and 0.8 mm, respectively. The fitting parameters also agree well with the parameters used in Section 2.3.5.

Understanding Gouy phase shift in ABCD provides an important guidance of electrodes design to optimize the detection efficiency and bandwidth. The long electrodes will have an average effect since the generated second harmonic along z-axis will add up coherently. Especially for those second harmonic photons with opposite phases, a cancellation will be introduced due to the destructive interference. To maintain a better phase match condition, thin electrodes that match Rayleigh range of terahertz beam is recommended in ABCD systems.

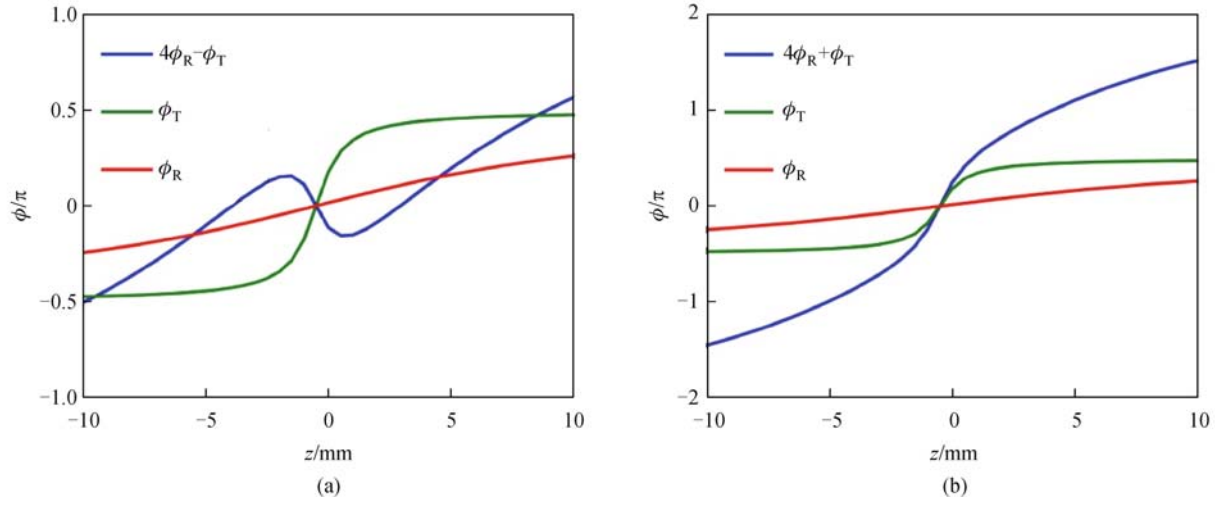

Fig. 11 Calculated Gouy phase shift corresponding to (a) $\omega+\omega-\Omega$ and (b) $\omega+\omega+\Omega$ process during ABCD. z is the longitudinal position along beams' propagation direction. Zero position is the focus position. Rayleigh ranges of terahertz beam and optical probe beam are 0.8 and 4.8 mm, respectively. Green, red and blue curves represent the phase change of terahertz waves, optical beams and phase difference between the two, respectively

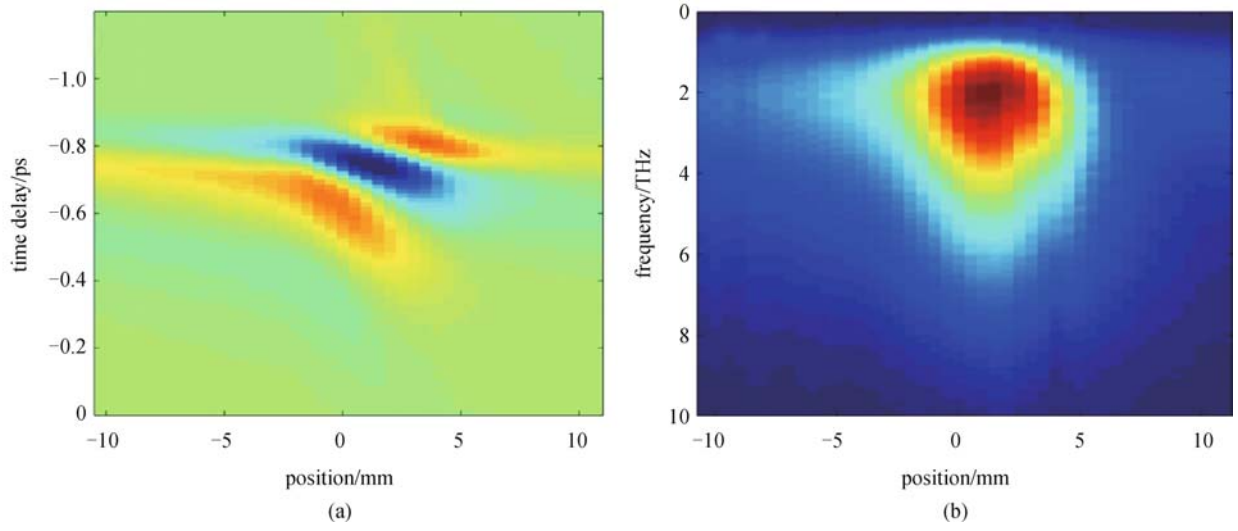

Fig. 12 Measured terahertz (a) waveforms and (b) spectra at various electrodes position along z-axis using ABCD

2.3.7 Pulse duration

Without phonon absorption, the detectable bandwidth of ABCD is only limited by the laser pulse duration. Figure 14 shows a series of ABCD measurements with various pulse durations. Sub-20 fs pulses can be obtained by compressing 35 fs pulses with a hollow fiber pulse compressor. The 35 fs pulses are spectrally broadened in a commercial hollow-core fiber (Femtolasers Kaleidoscope) filled with Ne gas (830 torr) to achieve a bandwidth sufficient to support sub-20 fs pulses, followed by re-compression with three pairs of chirped mirrors. A pulse-energy throughput above 40% is preserved with 600 μJ input pulse energy. With sub-20 fs pulses, the 10% bandwidth covers from 0.3 to 46 THz. The dip at 18 THz is the two-photon absorption of silicon wafer that is used to block residue optical beam. The details of ABCD with ultra-short pulses will be discussed in Section 4.

2.3.8 Figure of merit (FOM)

To conclude this section, we have collected the most relevant parameters of gases used for broadband terahertz wave detection in Table 1. Since directly measured n_{400}

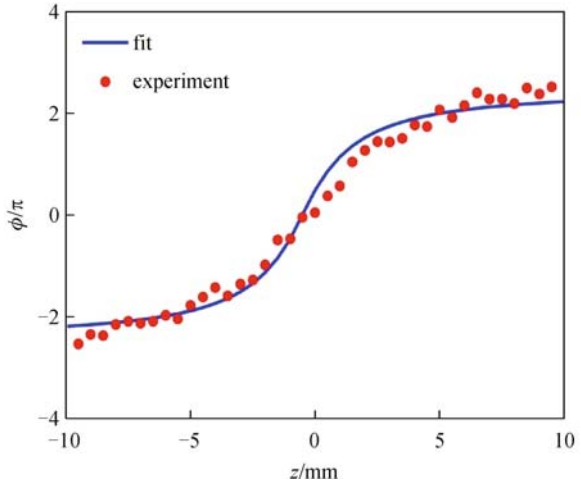

Fig. 13 Extracted phase information from measurements together with a theoretical fit. Rayleigh ranges of optical probe beam and terahertz beam are estimated to be 1.5 and 0.8 mm, respectively

and n_{800} values are available only for select materials, only these values are listed in the table. According to Table 1, at room temperature xenon has the highest FOM value. In our experiment, this gas can be used to detect terahertz pulses with an order higher signal in the cell. This result was achieved by using 50 μJ probe pulse energy, 14 kV/cm bias, and 756 torr pressure. However, based on our other tests, propane is the best gaseous sensor which can achieve 40 times higher signal compared to air with 40 μJ probe pulse energy, 30 kV/cm bias, and 700 torr pressure.

3 Balanced terahertz wave air-biased-coherent-detection (ABCD)

3.1 Introduction

In the past decades, terahertz time domain spectroscopy (TDS) has been widely applied into versatile fields, such as homeland security, material characterization, ultrafast dynamic process study, and biologic science. However, the system bandwidth is often limited by detection scheme. A simultaneous coherent and broadband detection scheme is a challenge in terahertz community. Unlike solid-state detectors, gases, which have no phonon resonance, better phase matching and continuous renewability, have been introduced as a flawless detection medium by providing an ultra-broadband coverage from 0.3 to 30 THz. However, compared to electro-optics sampling [72] or photoconductive antenna, which are commonly used in THz-TDS, the dynamic range and signal-to-noise ratio of gaseous sensors are relatively low because the mechanism is based on a third order nonlinear response of gaseous media. For any detection scheme, the dynamic range and signal-to-noise ratio are the principle factors for performance description. Improving dynamic range and signal-to-noise ratio can greatly reduce the acquisition time and also enhance the sensitivity of a system. In a conventional terahertz-ABCD [52] system, the electronic noise, dark current of the PMT detector, and laser fluctuation have been identified to limit the dynamic range and signal-to-noise ratio of the system. Especially, the noise from laser fluctuation has been recognized to be the primary noise source. As we discussed in Section 2, selecting efficient gases and optimizing detection efficiency provide approaches to greatly enhance signal to improve dynamic range, yet lack noise suppression [57].

In this section, we first discuss the noise in ABCD system and then introduce a balance detection scheme based on conventional THz-ABCD. A balanced heterodyne detection method for broadband terahertz waves using a polarization dependent geometry is demonstrated. Utilizing the tensor property of third order nonlinear susceptibility, second harmonic pulses with two orthogonal polarizations are detected by two separated PMTs. The signals from PMTs are subtracted with a balanced detection circuit to reduce the common noise from the offsets, yielding a factor of two improvement of signal-to-noise ratio.

3.2 Signal-to-noise ratio and dynamic range

In a terahertz TDS system, dynamic range and signal-to-noise ratio are the two principle factors for performance description. However, in terahertz community, there are no uniform definitions of dynamic range and signal-to-noise ratio until Ref. [73] came out. Here, we repeat the definitions in the following context for clarification. The signal-to-noise ratio of a terahertz TDS system is defined as the mean value of the peak amplitude divided by the standard deviation of that. The dynamic range is defined as the maximum magnitude of the amplitude divided by the rms of noise floor.

Based on this definition, the way to estimate the noise of the time-domain data can be obtained by evaluating the standard deviation of the peak signal fluctuation and that of the noise in the absence of terahertz signal. The former is obtained by fixing the delay at the peak maximum, while for the latter the delay is set to record the residual noise signal prior to the arrival of the terahertz pulse. The signal-to-noise ratio is then given by the ratio of the mean peak signal to its standard deviation, while the dynamic range is the ratio of the mean peak to the standard deviation of noise [73].

In a THz-TDS system, the broadly accepted noise sources are laser fluctuation, dark current from PMT and the bias field fluctuation. To understand the key factors affecting dynamic range and signal-to-noise ratio, in the following content, we will derive the dynamic range and signal-to-noise ratio in a terahertz ABCD system and discuss the optimization through adjusting gain of PMT or

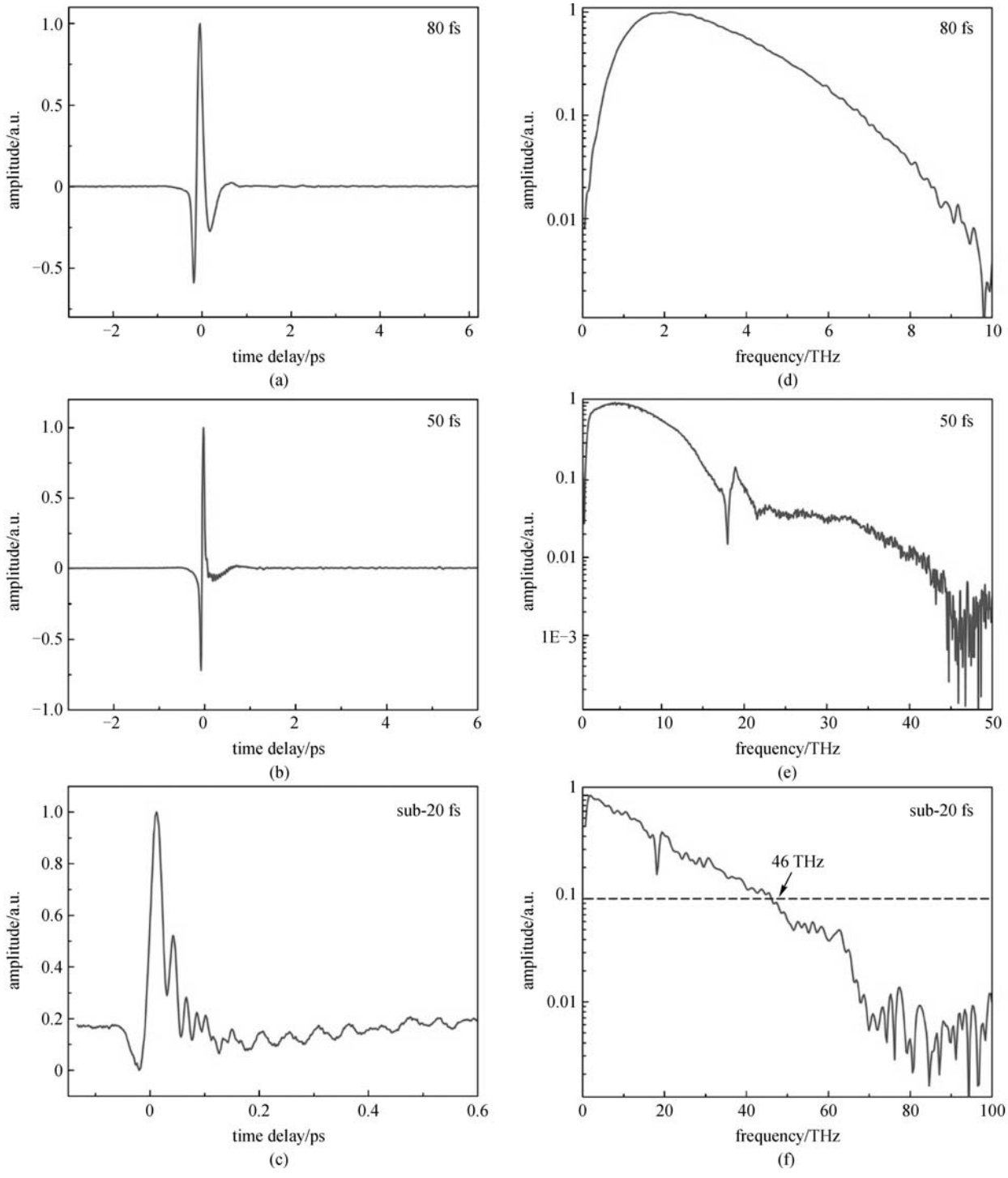

Fig. 14 Terahertz waveforms and spectra obtained with (a) and (d) 80 fs; (b) and (e) 50 fs; (c) and (f) sub-20 fs laser pulses

applied DC field.

As we derived in Section 2, theoretically, the output signal (S_o) from PMT can be written as

$$S_o = \left(\chi^{(3)} I_\omega\right)^2 (E_{DC} \pm E_{THz})^2. \quad (25)$$

The subscript represents the original signal input into lock-in amplifier. However, since the lock-in amplifier only detects the signal at modulation frequency, the actually readout signal (S) from lock-in amplifier is

$$S = 2[\chi^{(3)} I_\omega]^2 E_{DC} E_{THz}. \quad (26)$$

The background (B) signal then is defined as when there

Table 1 Properties of a few gases suitable for terahertz wave detection

	$\chi_0^{(3)}/\chi_0^{(3)}(N_2)$ [63]	$-dk/m^{-1}$ [67]	IP/eV [71]	FOM/FOM(N_2)
N_2	1	119	15.58	1
Ar	1.1	112	15.76	1.37
CH_4	2.8	259	12.61	1.66
Kr	3.0	229	14.00	2.43
Xe	7.5	542	12.13	2.69

is no terahertz signal, which is $E_{THz} = 0$.

$$B = \left(\chi^{(3)} I_\omega E_{DC}\right)^2. \tag{27}$$

Here, if we only consider laser fluctuation, which is the main noise in ABCD. The noise of background due to laser fluctuation δI_ω can be written as

$$\frac{\partial B}{\partial I_\omega}\delta I_\omega = 2\left(\chi^{(3)} E_{DC} I_\omega\right)^2 N_\omega. \tag{28}$$

Term $N_\omega = \dfrac{\delta I_\omega}{I_\omega}$ is actually the percentage of laser fluctuation, which is determined by the performance of laser system.

And the noise of peak signal can be derived in a similar approach, which can be expressed as

$$\frac{\partial S_o}{\partial I_\omega}\delta I_\omega = 2\left(\chi^{(3)} I_\omega\right)^2 (E_{DC} \pm E_{THz})^2 N_\omega. \tag{29}$$

Please note that, in this equation, we used original signal S_o instead of readout signal S. We made this variance because lock-in amplifier is based on the homodyne detection, which only gives the readout at reference frequency. Thus, when performing dynamic range or signal-to-noise ratio measurements, our measured signal is always the readout signal S. However, the noise has a relatively broad frequency spectrum. Thus, all terms in original signal will contribute to final measured noise.

The expression of dynamic range (DR) and signal-to-noise ratio (SNR) in an ABCD system thus can be finalized below.

$$DR = \frac{S}{\dfrac{\partial B}{\partial I_\omega}\delta I_\omega} = \frac{E_{THz}}{E_{DC}}\frac{1}{N_\omega}, \tag{30}$$

$$SNR = \frac{S}{\dfrac{\partial S_o}{\partial I_\omega}\delta I_\omega} = \frac{1}{N_\omega}\frac{E_{DC}E_{THz}}{(E_{DC}+E_{THz})^2} \leqslant \frac{1}{2N_\omega}. \tag{31}$$

Equations (30) and (31) point a clear direction to improve the system performance. Thus, the dynamic range and signal-to-noise ratio of an ABCD system are only limited by the applied DC field strength and laser fluctuation. Especially, only when the DC field strength is equal to the terahertz field strength, the optimal signal-to-noise ratio is achieved.

It is worthy to notice that Eqs. (30) and (31) are based on a simplified estimation, which is not true in the real system. In a real terahertz system, other noise source, including detector and electronic noise, needs to be considered. Taking DC field fluctuation and noise equivalent power (NEP) of detectors into consideration, the dynamic range and signal-to-noise ratio can be derived in a similar approach.

The noise of background due to DC field fluctuation δE_{DC} can be written as

$$\frac{\partial B}{\partial E_{DC}}\delta E_{DC} = 2\left(\chi^{(3)} I_\omega E_{DC}\right)^2 N_{DC}, \tag{32}$$

where $N_{DC} = \dfrac{\delta E_{DC}}{E_{DC}}$ is the percentage of fluctuation of bias field, which is only determined by the performance of our high voltage modulator. And the noise of peak signal can be derived in a similar approach, which can be expressed as

$$\frac{\partial S_o}{\partial E_{DC}}\delta E_{DC} = 2\left(\chi^{(3)} I_\omega\right)^2 \left(1 + \frac{E_{THz}}{E_{DC}}\right) N_{DC}. \tag{33}$$

The overall expression of dynamic range (DR) and signal-to-noise ratio (SNR) in an ABCD system thus can be finalized below.

$$DR = \frac{S}{\sqrt{\left(\dfrac{\partial B}{\partial E_{DC}}\delta E_{DC}\right)^2 + \left(\dfrac{\partial B}{\partial I_\omega}\delta I_\omega\right)^2 + NEP^2}} = \frac{2[\chi^{(3)} I_\omega]^2 E_{DC} E_{THz}}{\sqrt{4\left(\chi^{(3)} I_\omega E_{DC}\right)^4 (N_{DC}^2 + N_\omega^2) + NEP^2}}, \tag{34}$$

$$SNR = \frac{S}{\sqrt{\left(\dfrac{\partial S_o}{\partial E_{DC}}\delta E_{DC}\right)^2 + \left(\dfrac{\partial S_o}{\partial I_\omega}\delta I_\omega\right)^2 + NEP^2}} = \frac{2[\chi^{(3)} I_\omega]^2 E_{DC} E_{THz}}{\sqrt{4\left(\chi^{(3)} I_\omega\right)^4 \left(\dfrac{1}{E_{DC}^2 (E_{THz}+E_{DC})^2} N_{DC}^2 + N_\omega^2\right) + NEP^2}}. \tag{35}$$

Equations (34) and (35) point a clear direction to improve the system performance, although the noise in a real system is much more complicated. From Eqs. (34) and (35), the dynamic range and signal-to-noise ratio reduce if

the fluctuations of applied DC field or laser increase, which is intuitively correct. Furthermore, the field strength of applied DC field and probe pulse energy also play important role in optimizing system performance. The calculated trend of dynamic range and signal-to-noise ratio with respect to the probe pulse energy (I_ω) or DC field strength (E_{DC}) in the ABCD is plotted in Fig. 15.

3.2.1 Gain of photomultiplier tube (PMT)

The PMT detector is a vacuum tube that contains a photocathode, a number of dynodes and an anode, which delivers the output signal. The released photoelectrons from photocathode hit on a series of dynodes and an amplification of the signal is achieved through this process. This amplification process can be controlled by the applied external high voltage, which is called the gain of PMT. Thus, PMT is an extremely sensitive detector, which could even achieve single photon detection.

In a PMT detector, the output current signal is amplified by the gain while the noise is also amplified. Moreover, even if there is absolutely no incident photon, the PMTs still have an intrinsic output current, which is commonly called dark current. Figure 16 shows the typical trend of signal output and dark current versus the gain voltage. The causes of dark current are beyond the scope of this study, which will not be detailed here. In the figure, the output characters can be separated into three regions: region a is dominated by dark current; region b is called linear region where best signal-to-noise ratio is obtained; region c is the high voltage region where a dramatic increase of field emission current is observed. Selecting correct gain of PMT will affect our measured signal-to-noise ratio significantly.

We performed a dynamic range and signal-to-noise ratio analysis with respect to the gain level of PMT in an ABCD system. Figure 17 shows the measurement results. It is clear that the dynamic range and signal-to-noise ratio in a conventional ABCD system inevitably vary with the gain of PMT. Initially, when dark noise is dominated, the dynamic range increases dramatically due to the amplification of signal. However, the signal-to-noise is not very sensitive to the gain of PMT in this region. With the entry into linear region, the dynamic range reaches optimal condition and the signal-to-noise also starts to increase. If the PMT is working in high voltage region, the dramatically increased dark current limits both dynamic range and signal-to-noise ratio.

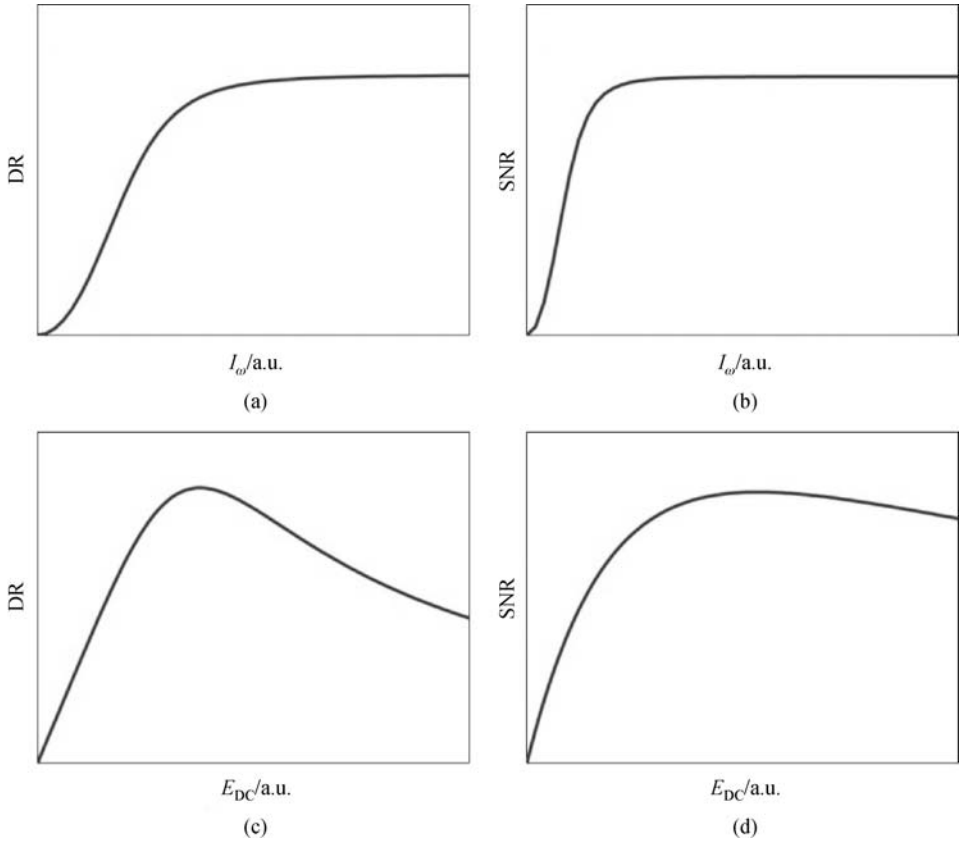

Fig. 15 Calculated trend of (a) and (c) dynamic range (DR); (b) and (d) signal-to-noise ratio (SNR) with respect to (a) and (b) probe pulse energy (I_ω); (c) and(d) DC field strength (E_{DC}) in ABCD system

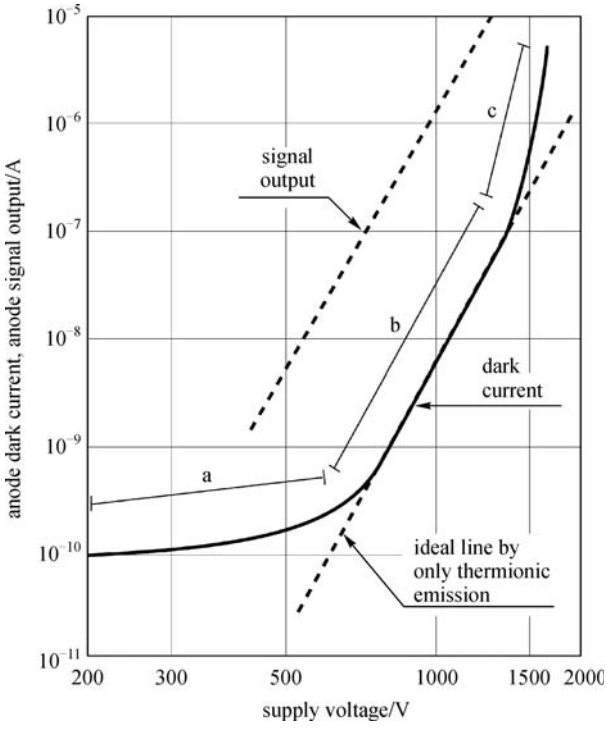

Fig. 16 Typical signal output and dark current vs. supply voltage (gain voltage) of a PMT (Courtesy Hamamatsu Photonics K.K.)

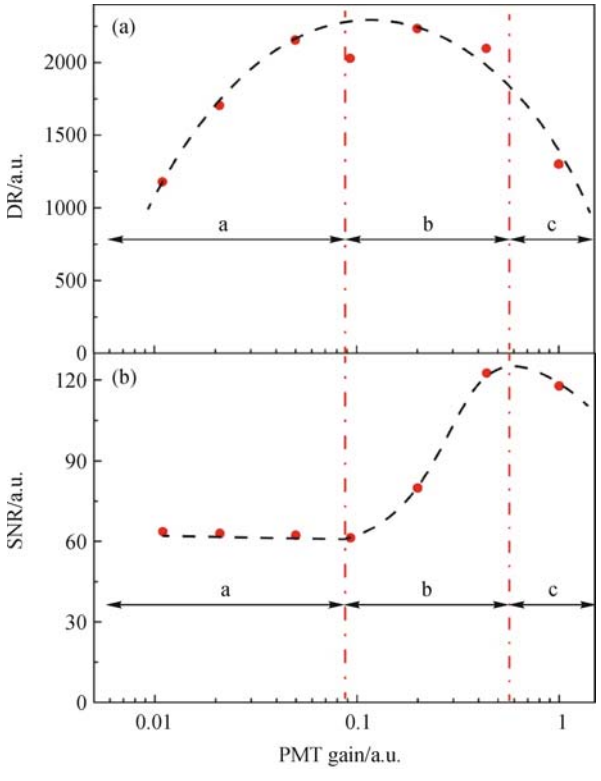

Fig. 17 Comparison of (a) dynamic range (DR) and (b) signal-to-noise ratio (SNR) with respect to the gain of PMT. Red dots are measured experimental data and dashed black curves are the guide for the eye

Understanding the characteristics of our detector provides us the first approach to optimize our system. To achieve the best system performance, the PMT should work at linear region through gain adjustment.

3.2.2 Bias field

According to Eqs. (34) and (35), the applied DC field strength on detection region will greatly affect the system performance, although they are not completely correct due to the complexity of noise sources. We performed the measurements of dynamic range and signal-to-noise ratio with respect to the biased field strength in an ABCD system, which is shown in Fig. 18.

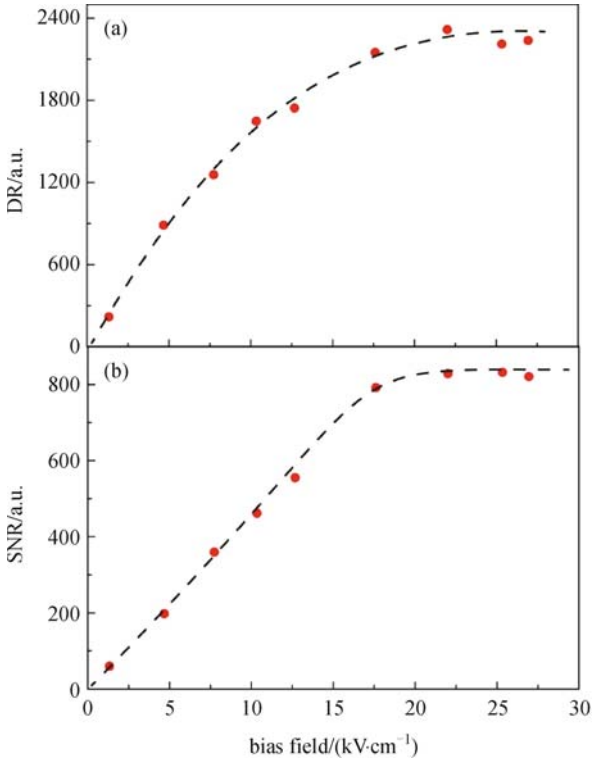

Fig. 18 Comparison of (a) dynamic range (DR) and (b) signal-to-noise ratio (SNR) with respect to bias field strength. Blacked dashed lines are the guides for the eyes

3.3 Balanced terahertz wave air-biased-coherent-detection (ABCD)

As we discussed in Section 2, conventional THz-ABCD uses a concept of heterodyne detection: introducing a modulated bias field-induced second harmonic as the local oscillator, mixing terahertz field-induced second harmonic with the local oscillator through interference, and finally isolating the cross term at modulation frequency through a lock-in amplifier. Based on the lock-in technique, the DC offset terms will be automatically ignored. However, the

noises from these terms still limit the signal-to-noise ratio and even saturate the lock-in amplifier. In early works with optical heterodyne detection or electro-optic sampling techniques, a balanced detection scheme is utilized based on a polarization geometry, which minimizes laser fluctuation down to the laser or photodiode shot noise limit.

The balanced ABCD scheme is achieved by utilizing the isotropic tensor property of $\chi^{(3)}$ in gases. In an isotropic media, the third-order susceptibility tensors have 21 nonzero components, of which only 3 are independent [64]. If we ignore the properties in z direction, the independent nonzero tensors reduced to: $\chi^{(3)}_{yyxx}$, $\chi^{(3)}_{xyxy}$, $\chi^{(3)}_{xyyx}$ and $\chi^{(3)}_{xxxx}=\chi^{(3)}_{yyxx}+\chi^{(3)}_{xyxy}+\chi^{(3)}_{xyyx}$ with the four subscripts corresponding to polarizations of 2ω, terahertz field (or bias field), ω, and ω beams, respectively. To produce a differential signal, we select two $\chi^{(3)}$ elements: $\chi^{(3)}_{xxxx}$ and $\chi^{(3)}_{yyxx}$. $\chi^{(3)}_{xxxx}$ represents that all four waves are in x polarization, and $\chi^{(3)}_{yyxx}$ represents that 2ω, terahertz field (or bias field) in y polarization, while fundamental beam ω is x polarization. Thus, if the polarization of terahertz field is oriented at certain angle with respect to the polarization of ω beam, the produced 2ω beam will have two orthogonal components.

Figure 19 shows a schematic of balanced ABCD for broadband terahertz waves. The detection scheme is similar to conventional terahertz ABCD. However, the polarization of each beam is controlled separately and rotated to certain angle with respect to each other, which is shown in the gray circle of Fig. 19.

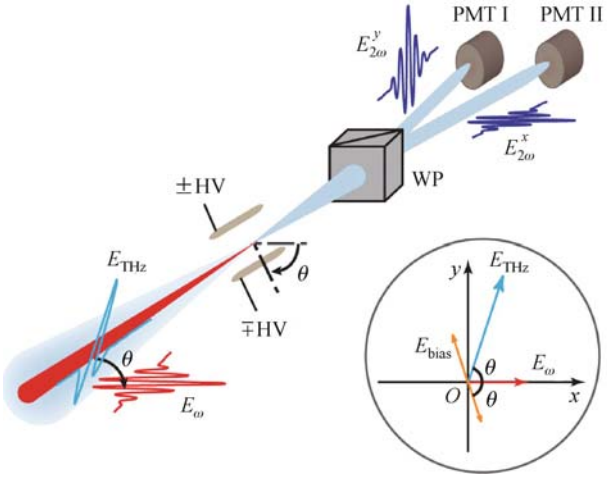

Fig. 19 Schematic of balanced ABCD for terahertz waves. WP: Wollaston prism. PMT: photomultiplier tube. The polarization of each beam and the experimental coordinate are shown inside the gray circle

In the x direction (p-polarized) and y direction (s-polarized), the total second harmonic field is equal to the combination of both terahertz and bias field-induced second harmonic fields,

$$E^x_{2\omega}=(E^{\mathrm{THz}}_{2\omega})_x\pm(E^{\mathrm{bias}}_{2\omega})_x \propto \chi^{(3)}_{xxxx}I_\omega E_{\mathrm{THz}}\cos\theta\pm\chi^{(3)}_{xxxx}I_\omega E_{\mathrm{bias}}\cos\theta, \tag{36}$$

$$E^y_{2\omega}=(E^{\mathrm{THz}}_{2\omega})_y\mp(E^{\mathrm{bias}}_{2\omega})_y \propto \chi^{(3)}_{yyxx}I_\omega E_{\mathrm{THz}}\sin\theta\mp\chi^{(3)}_{yyxx}I_\omega E_{\mathrm{bias}}\sin\theta, \tag{37}$$

where $E^x_{2\omega}$ and $E^y_{2\omega}$ are the total second harmonic electrical field along x and y-axis, I_ω is the intensity of fundamental beam, and E_{THz}, E_{bias} are the amplitude of terahertz field and bias field. The superscript is corresponding to terahertz field or bias field, respectively. Due to the phase modulation of the bias-induced second harmonic, the difference in carrier phases between $E^{\mathrm{THz}}_{2\omega}$ and $E^{\mathrm{bias}}_{2\omega}$ is either 0 or π, resulting an alternating sign in Eqs. (36) and (37).

Due to the response of our detector, the signal we measured in detection is actually proportional to the intensity of second harmonic beams.

$$I^x_{2\omega}\propto\left(\chi^{(3)}_{xxxx}I_\omega\cos\theta\right)^2(E_{\mathrm{THz}}\pm E_{\mathrm{bias}})^2, \tag{38}$$

$$I^y_{2\omega}\propto\left(\chi^{(3)}_{yyxx}I_\omega\sin\theta\right)^2(E_{\mathrm{THz}}\mp E_{\mathrm{bias}})^2. \tag{39}$$

To achieve a balanced signal in this differential geometry, we choose to satisfy $\chi^{(3)}_{xxxx}\cos\theta=\chi^{(3)}_{yyxx}\sin\theta=A$. Thus, the detected signal from each detector can be expressed as

$$I^x_{2\omega}\propto A^2I^2_\omega[(E_{\mathrm{THz}})^2+(E_{\mathrm{bias}})^2\pm2E_{\mathrm{THz}}E_{\mathrm{bias}}], \tag{40}$$

$$I^y_{2\omega}\propto A^2I^2_\omega[(E_{\mathrm{THz}})^2+(E_{\mathrm{bias}})^2\mp2E_{\mathrm{THz}}E_{\mathrm{bias}}]. \tag{41}$$

By subtracting one from another, the output signal could be expressed as

$$I_{2\omega}=I^x_{2\omega}-I^y_{2\omega}\propto\pm4A^2I^2_\omega E_{\mathrm{THz}}E_{\mathrm{bias}}. \tag{42}$$

If we compare Eq. (42) with Eq. (6) for conventional ABCD, although the signal reduces by a factor of $A^2/2$, the noise from offset terms are completely removed, which provide a possibility to enhance the signal-to-noise ratio.

3.4 Experimental results

3.4.1 Experimental setup

Figure 19 illustrates a geometric scheme of balanced terahertz ABCD with the experimental coordinate shown in a gray circle. The experiment was performed with a Coherent Libra HE Ti:Sapphire amplified laser system,

which can deliver laser pulses with 800 nm wavelength, 50 fs duration, 1.4 mJ energy at a 3 kHz repetition rate. The laser pulses were separated into pump (1.06 mJ) and probe (40 μJ) beams to generate and detect terahertz waves, respectively. The terahertz wave was generated by focusing both the fundamental and second harmonic beams with a 150 mm lens to ionize air. The radiated terahertz wave was collected by a 90° off-axis parabolic mirror and focused again by another parabolic mirror. The probe beam was sent through a time-delay stage and then focused by a 150 mm lens through a hole in the final parabolic mirror. Thus, the terahertz wave propagated collinearly with the probe beam and was focused at the same location. To produce second harmonic beams in both x and y direction, the terahertz beam was optimized to a linear polarization with an angle of θ as shown in Fig. 19 by rotating the polarization of pump beam. The electrodes were positioned at the focus and the electrical field was oriented at an angle of θ with respect to the polarization of probe beam. The second harmonic beam passed through a pair of 400 nm bandpass filters, split into x and y components by a Wollaston prism with 400 nm AR coating and detected by two PMTs. The bias field was provided by a high voltage modulator, which delivers bipolar square waves with a frequency of 500 Hz and an amplitude of ±1.5 kV. The output signals from both PMTs went through a current subtracter and the differential signal was detected by the lock-in amplifier with a reference frequency of 500 Hz.

A detailed diagram of current subtractor is shown in Fig. 20**.** P1 and P2 are corresponding to the outputs from two individual PMTs. The transistors R1 and R2 converted current signal into voltage and input into AD 820. The function of AD 820 is to perform subtraction of two inputs. The output is sent through a RC low pass filter, which designed to operate at 1 kHz, to further improve signal-to-noise ratio.

In most of gases, $\chi^{(3)}_{xxxx} = 3\chi^{(3)}_{yyxx}$ [74–76], which leads to $\theta \approx 71.6°$. This angle also can be easily measured and estimated in our experiment through comparing through comparing DC field induced second harmonic by blocking the terahertz beam. The angle measured in our experiment is around $70° \pm 1°$, which is within the range of experimental error.

3.4.2 Demonstration of balanced air-biased-coherent-detection (ABCD)

Based on Eqs. (40) and (41), the cross terms in $I^x_{2\omega}$ and $I^y_{2\omega}$ have opposite signs. This means that if we measure individual component from each PMT, the signal detected will have a π phase difference. Figure 21 shows detected terahertz waveforms with individual $I^x_{2\omega}$ and $I^y_{2\omega}$ component of second harmonic. The balanced signal $(I^x_{2\omega} - I^y_{2\omega})$ is obtained by using a current subtraction circuit. Figure 21 demonstrates the concept of balanced ABCD. By introducing a polarization dependent geometry, two out of phase signals are detected separately by two detectors. In this case, a subtraction will help to reduce the noise fluctuation since the background noise is correlated while maintaining the signal.

3.4.3 Comparison of dynamic range and signal-to-noise ratio

After conceptual demonstration of balanced ABCD, we performed a comparison experiment between conventional ABCD and balanced ABCD. In our experiments, the gain for each PMT was first calibrated with the same second harmonic source. It is worthy to note that the balance between $I^x_{2\omega}$ and $I^y_{2\omega}$ is achieved by proper polarization orientations instead of electrical amplification of each signal. The measurements with conventional terahertz ABCD system are performed with all the beams' polarization in x direction while maintaining all other

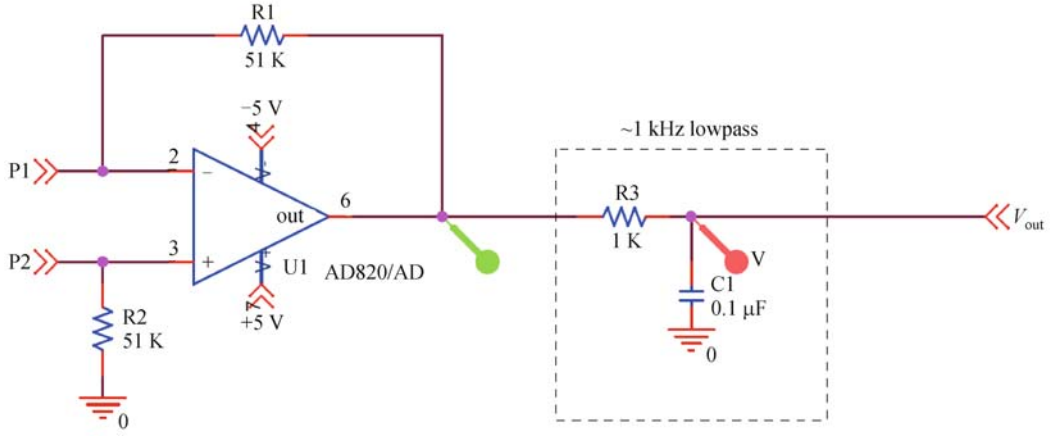

Fig. 20 A circuit diagram of current subtractor. Current outputs from two PMTs (P1 and P2) are sent through an analogy device AD 820, which can provide a output proportional to the subtraction between P1 and P2 (Courtesy Dr. Brian Schulkin)

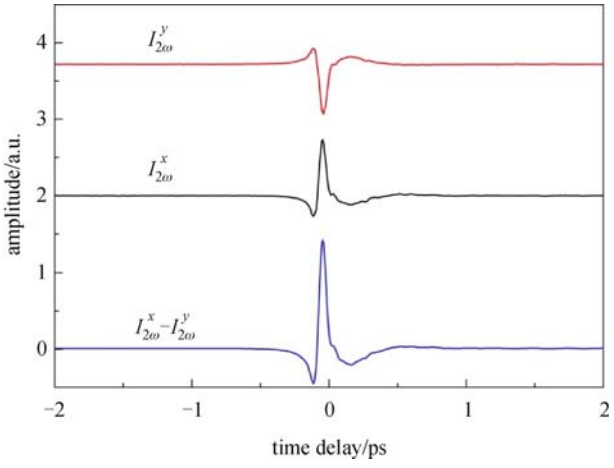

Fig. 21 Each component measured in balanced ABCD. Waveforms are offset vertically for clarity

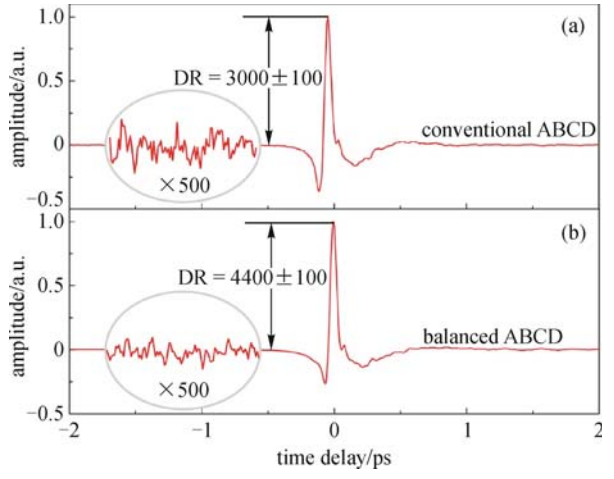

Fig. 22 Comparison of measured dynamic ranges (DRs) between (a) conventional ABCD and (b) balanced ABCD. Background fluctuations with a 500 times magnification are shown in gray circles. Waveforms are normalized with peak values. Waveforms are obtained with a lock-in time constant of 100 ms and a total of 9 scans

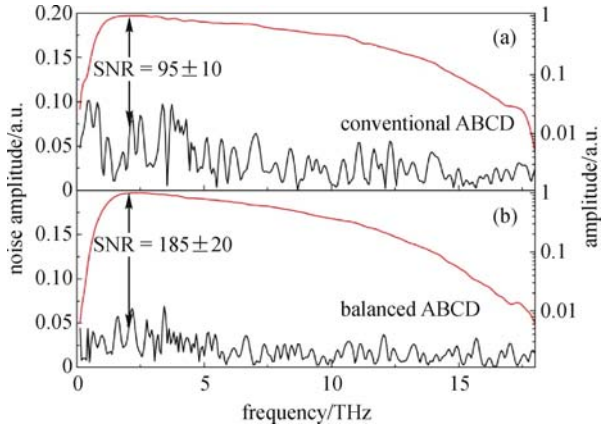

Fig. 23 Comparison of measured signal-to-noise ratio (SNR) between (a) conventional ABCD and (b) balanced ABCD. Terahertz spectra and noise floors are shown in red and black lines, respectively. Signals were obtained with a lock-in time constant of 100 ms and a total of 9 scans

experimental circumstances the same. The dynamic range of ABCD system is defined as the maximum quantifiable. Here, we use the definition of dynamic range and signal-to-noise ratio from Ref. [73]. Figure 22 shows a comparison of dynamic ranges between each method. The dynamic range is recorded by evaluating the standard deviation of the noise in the absence of terahertz signal (the delay is set to record the noise signal 1 ps prior to the arrival of the terahertz pulse).

Figure 23 shows a comparison of signal-to-noise ratio between conventional ABCD and balanced ABCD. The signal-to-noise ratio can be obtained by evaluating the standard deviation of the peak signal by fixing the delay at the peak maximum. The measurements reveal that balanced ABCD provides the ability for noise cancellation that significantly improves dynamic range and signal-to-noise ratio.

If only considering the noise introduced by laser fluctuation, the dynamic range and signal-to-noise ratio of an ABCD system can be derived theoretically, which is listed in Table 2. The signal (S) is the 500 Hz cross term read by lock-in amplifier, which we only consider the case with "+." The background fluctuation is defined as standard deviation of background signal in the absence of terahertz field ($E_{\mathrm{THz}} = 0$) and the noise is defined as the standard deviation of terahertz peak signal with respect to laser fluctuation. From Table 2, we noticed that, in balanced ABCD, a great reduction of background fluctuation is achieved. Theoretically, the dynamic range could be enhanced infinitely if the offset terms can be completely removed. Moreover, since the inequality $\frac{I_\omega E_{\mathrm{THz}} E_{\mathrm{bias}}}{\delta I_\omega (E_{\mathrm{THz}} + E_{\mathrm{bias}})^2} \leqslant \frac{I_\omega}{2\delta I_\omega}$ always holds, an enhancement of signal-to-noise ratio with balanced ABCD is also expected.

4 Ultra-broadband terahertz generation and detection

4.1 Introduction

Ambient air, while excited with ultrashort laser pulses, has been demonstrated as an intense and broadband terahertz source. Early in 1990s, Hamster et al. obtained sub-pico second terahertz radiation by focusing intense laser pulses to ionize air and the mechanism was reported as electron-ion dipole radiation induced by laser pondermotive force

Table 2 Theoretical comparison of signal-to-noise ratio and dynamic range between conventional ABCD and balanced ABCD

	conventional ABCD	balanced ABCD
signal (S)	$2I_\omega^2 E_{\mathrm{THz}} E_{\mathrm{bias}}$	$4A^2 I_\omega^2 E_{\mathrm{THz}} E_{\mathrm{bias}}$
background fluctuation ($E_{\mathrm{THz}} = 0$)	$2I_\omega \delta I_\omega (E_{\mathrm{bias}})^2$	$\rightarrow 0$
noise ($E_{\mathrm{THz}} \neq 0$, $\frac{\partial S}{\partial I_\omega}\delta I_\omega$)*	$2I_\omega \delta I_\omega [(E_{\mathrm{THz}})^2 + (E_{\mathrm{bias}})^2 + 2E_{\mathrm{THz}}E_{\mathrm{bias}}]$	$8A^2 I_\omega \delta I_\omega E_{\mathrm{THz}} E_{\mathrm{bias}}$
signal-to-noise ratio	$\frac{I_\omega E_{\mathrm{THz}} E_{\mathrm{bias}}}{\delta I_\omega [(E_{\mathrm{THz}})^2 + (E_{\mathrm{bias}})^2 + 2E_{\mathrm{THz}}E_{\mathrm{bias}}]}$	$\frac{I_\omega}{2\delta I_\omega}$
dynamic range	$\frac{E_{\mathrm{THz}}}{E_{\mathrm{bias}}}\frac{I_\omega}{\delta I_\omega}$	$\rightarrow \infty$

Note: * The noise is defined as the standard deviation of terahertz peak signal with respect to laser fluctuation

[34]. Later, Cook et al. optimized the terahertz radiation from laser-induced plasma by mixing fundamental beam with its second harmonic to ionize air, which was claimed as a four wave mixing process in air [36,77]. The underlying mechanism and physics for terahertz generation from air plasma have been debating for years. Recently, both semi-classical transient current model [78,79] and quantum mechanical model [80,81] have been established, demonstrating that the terahertz emission is related to the driven motion of ionized electrons under intense electrical field during the photo-ionization process. However, if the pulse during is short down to a few cycles, the carrier envelope phase plays important role on the ionized electron current. Kreß et al. showed that few-cycle pulses can directly produce a spatial charge asymmetry in the plasma. The asymmetry, associated with terahertz emission, depends on the carrier envelope phase, which allows for a determination of the carrier-envelope phase by measuring the amplitude and polarity of the terahertz pulse [82].

In this section, the terahertz wave generation and detection with ultra-short pulses are studied. The effects associate with carrier envelope phase and phase match in BBO are discussed. Moreover, an ultra-broadband terahertz wave with a bandwidth covering up to 70 THz is generated and detected experimentally.

4.2 Few-cycle pulses techniques

4.2.1 Carrier-envelope phase

The temporal profile of an ultra-short pulse can be described as

$$E(t) = \exp\left(-\frac{t^2}{\tau^2}\right) \mathrm{e}^{-\mathrm{i}\omega t} \mathrm{e}^{\mathrm{i}\phi}, \tag{43}$$

where $\exp\left(-\frac{t^2}{\tau^2}\right)$ presents the envelope of the pulse, $\mathrm{e}^{-\mathrm{i}\omega t}$ describes the oscillating electrical field and $\mathrm{e}^{\mathrm{i}\phi}$ is the phase offset between the envelope and the oscillating field, which is called carrier-envelope phase or absolute phase. τ is the pulse duration and ω is the center frequency. To summary, the carrier-envelope phase of a pulse is defined as the difference between the phase of the carrier wave and the envelope position, the latter being converted to a phase value.

Usually, carrier-envelope phase is not essential for long pulse duration. However, when the pulse duration is shorten to several cycles, carrier-envelope phase becomes important for pulse stabilization [83], especially for the coherent control of some carrier-envelope phase related process, such as photo-ionization [84], XUV generation [85] and atto-second science [86].

4.2.2 Hollow fiber pulse compressor

With the development of chirped pulse amplification technique [87], the commercialized amplified lasers can easily provide pulse energies in mJ and even joule levels with a pulse duration in tens of femtosecond range. But amplification of pulses with shorter durations even to the mJ level is a difficult task requiring complicated setups. Normally, intense laser pulses with duration down to few-cycle regimes can be achieved through pulse compression technique such as noble gas-filled hollow core fibers [88–90] and filamentation [91,92].

The hollow-fiber pulse compression technique has been broadly utilized in compressing high power femtosecond laser pulses down to few-cycle pulses [89]. While intense laser pulses are propagating through a hollow fiber filled with a noble gas, spectral broadening is induced by self-phase modulation due to Kerr and ionization effects. The spectrally broadened pulses can form few-cycle pulses after compensating for the chirp remained in output pulses.

Figure 24 shows a schematic of hollow fiber pulse compressor used in our experiment. The 35 fs pulses delivered from Coherent Legend Elite DUO are spectrally broadened in a commercial hollow-core fiber (Femtolasers Kaleidoscope) filled with Ne gas to achieve a bandwidth sufficient to support sub-7 fs pulses, followed by re-compression with three pairs of chirped mirrors. The

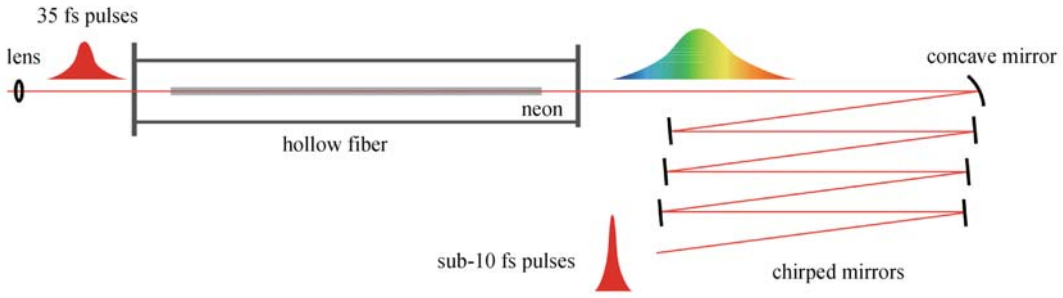

Fig. 24 Schematics of hollow fiber pulse compressor used in our experiment. 35 fs second laser pulses was input into a hollow core fiber placed in a neon-filled chamber. The self-phase modulation of intense laser pulses provides a sufficient bandwidth. Output pulses are compressed down to sub-10 fs by three pairs of chirped mirrors

length of hollow-core fiber is designed to be 1 m with a core diameter of 250 μm. Typically, a pulse-energy throughput above 40% is preserved but varies with input pulse energy.

In the hollow-core fiber pulse compressor, the output spectrum bandwidth can be controlled by varying input pulse duration, input pulse energy or gas pressure. The comparisons of the measured output pulse spectra with various input pulse energy and with different gas pressures are shown in Fig. 25. The characteristics of input pulse were measured with frequency-resolved optical gating (FROG) [93] technique and set to be 34 fs in pulse duration with a spectrum width of 22 nm (full width at half maximum, FWHM). Since the spectrum broaden is provided through a nonlinear self-phase modulation process when intense laser propagates in gaseous media, a significant broaden spectrum were observed by increasing input pulse energy (Fig. 25(a)). Limited by the safe operating pressure range of the chamber, the spectrum did not show a clear broadening effect while increasing pressure. However, the effect associated with the camber pressure cannot be ignored when compressing the pulses to few-cycle limits.

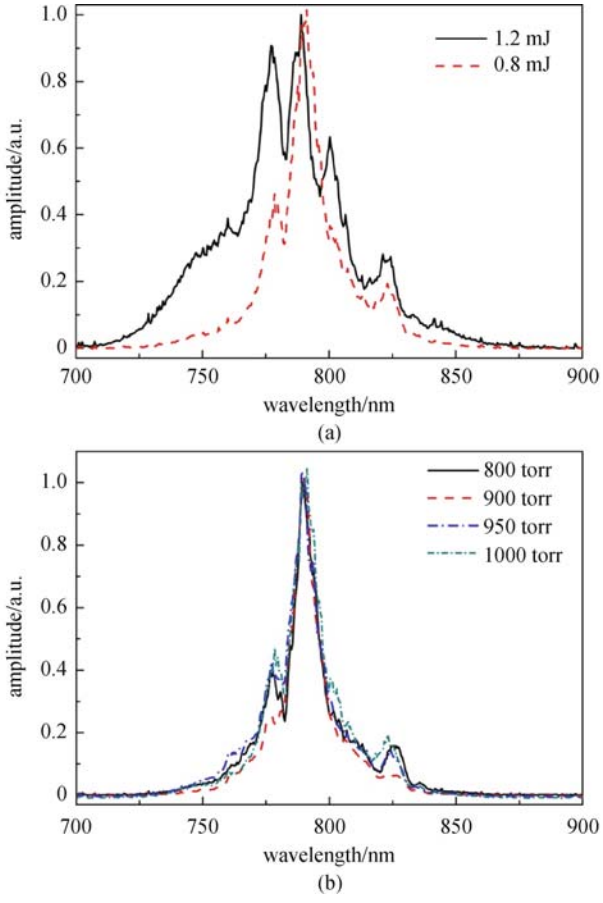

Fig. 25 Measured spectra of output pulses from hollow-core fiber pulse compressor with various (a) input pulse energy and (b) neon gas pressure in the chamber

4.3 Terahertz wave generation with few-cycle pulses

Although the air-plasma-based terahertz sources have been extensively studied these years due to its intense and broadband nature, the terahertz radiation from few-cycle pulses has not been reported until recently. Kreß et al. first reported that through monitoring the phase of emitted terahertz waves, the detailed information of carrier-envelope phase of few-cycle pulses can be accurately extracted [82], since the terahertz emission is essentially associated with the optical ionization process. Recently, Thomson et al. demonstrated that using two-color ($\omega - 2\omega$) optical field with a bandwidth supporting sub-20-fs duration to excite ambient air, the incommensurate optical field can radiate terahertz waves with a continuous bandwidth exceeding 100 THz and a pulse energy of 360 nJ [37]. In the following context, we will discuss the important parameters that substantially affect the terahertz generation with few-cycle pulses.

The experiment was performed with Coherent Legend Elite DUO Ti: Sapphire amplifier, which can deliver 35 fs pulses with a pulse energy up to 6.5 mJ at a repetition rate of 1 kHz. A commercial hollow-core fiber (Femtolasers

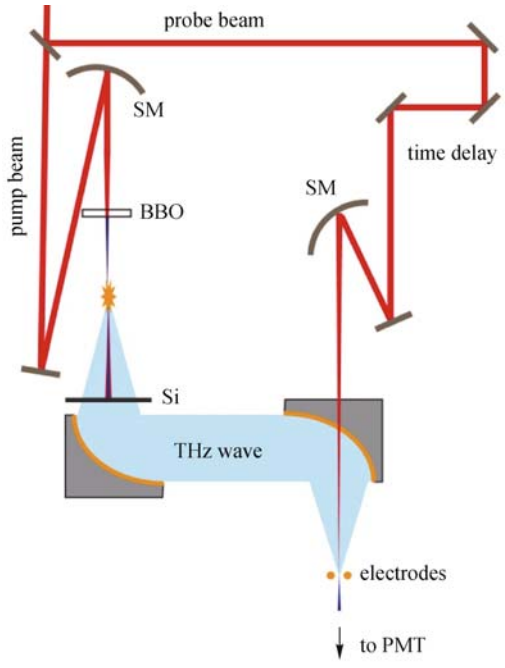

Fig. 26 Experimental setup of terahertz ABCD with few-cycle pulses. SM: spherical mirror. PMT: photomultiplier tube. A 60%–40% ultrafast beam splitter was used to separate laser pulses into optical pump pulses and optical probe pulses. The pump pulses were focused with a spherical mirror with 150 mm effective focal length to ionize ambient air. A 1 mm thick silicon wafer was used to block the residue optical beam. The optical probe beam went through a time delay stage and focused by another spherical mirror into the detection region

Kaleidoscope) filled with 800 torr Ne gas was used to compress the pulse to sub-20 fs or even shorter. The input pulse energy was 1 to 1.5 mJ and the throughput was about 40% after three pairs of chirped mirrors.

An experimental layout is shown in Fig. 26. To eliminate unnecessary dispersive effect from optics, metallic mirrors and spherical mirrors were used to replace dielectric mirrors and lenses that are typically used in a terahertz ABCD system. A 60%–40% ultrafast beam splitter was used to separate laser pulses into optical pump pulses and optical probe pulses. The pump pulses were focused with a spherical mirror with 150 mm effective focal length to ionize ambient air. A thin BBO crystal was inserted before the geometrical focus to produce second harmonic pulses. BBO crystals with various thicknesses at 50 and 30 μm were tested during our experiments.

From two-color plasma, the terahertz intensity linearly depends on the second harmonic intensity [36,77], making second harmonic conversion efficiency from BBO crystal an essential parameter for generation efficiency optimization. Particularly, few-cycle pulses are expected to possess relatively broad bandwidth, which causes critical phase matching inside BBO crystal. We investigated the generated terahertz field strength related to BBO thickness

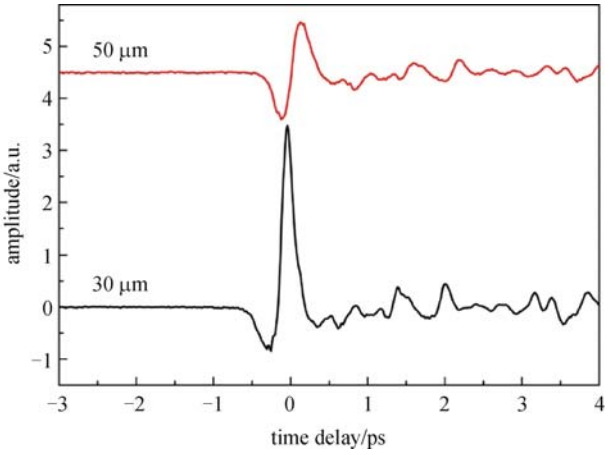

Fig. 27 Comparison of generated terahertz field strength with various BBO thicknesses. Electrical field strength was measured using a 100 μm GaP crystal

with our system. A 100 μm GaP crystal was used to calibrate the electrical field strength of emitted terahertz waves. The measured results are shown in Fig. 27. The experiments were performed with the same input pulse condition, in which the pulse duration was estimated to be around 15 fs. Moreover, the BBO crystals were rotated and moved along propagation direction to optimize signal for each case. It is clear that the signal strength obtained with 30 μm BBO crystal is more than twice greater than that with 50 μm BBO.

It is worth to note that another strong terahertz radiation was also detected in our experiment and verified to be from optical rectification in BBO crystal. Commonly, with longer pulse durations, the terahertz emission from BBO crystal is at least two orders lower than that from air plasma source. However, with few-cycle pulses, due to the high peak intensity, we measured a strong radiation from BBO crystal with pulse energy up to 50 nJ. Figure 28 shows a series of measured terahertz waveforms and corresponding spectra using ABCD with various input pulses characters. We notice that the spectrum has features between 10 to 30 THz, which does not predict from air generation. These spectral features are from terahertz wave components generated from optical rectification in BBO crystal. However, while increasing the input pulse energy, when the ionization is optimized for air-plasma source, the terahertz wave emitted from laser-induced plasma is dominated.

After optimizing the ABCD system, the best detectable terahertz radiation was obtained and shown in Fig. 29. The spectrum extends into mid-infrared regime and cuts off at around 70 THz. In time domain, the terahertz pulse duration is about 20 fs FWHM. The dip around 18 THz is from two phonon absorption in silicon wafer [94], which was used to block residue optical beam.

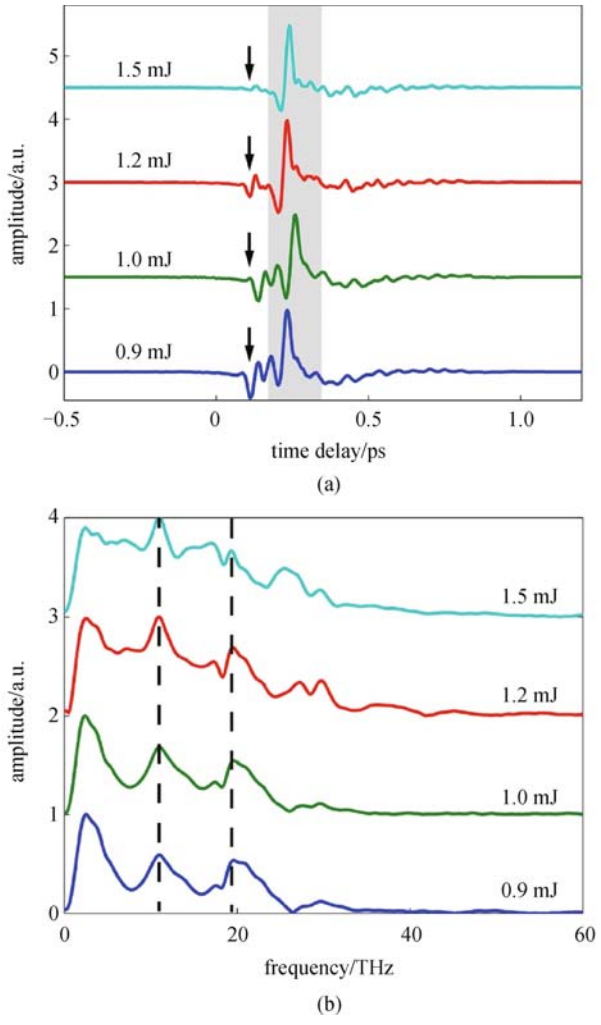

Fig. 28 Measured (a) waveforms and (b) spectra of ultra-broadband terahertz waves generated with ultra-short pulses with different input pulse energy

5 Generation of circularly polarized terahertz waves

5.1 Background

Electromagnetic pulses in the terahertz frequency range play a pivotal role in material spectroscopy, biomedical diagnosis and homeland security [1–3]. However, coherently exciting and controlling a circular polarized terahertz wave has proved to be a challenge, primarily because most terahertz sources are based on optical rectification or dipole radiation. Elliptically or circularly polarized terahertz waves are potentially important to study macromolecular chiral structures such as proteins and DNA or excite spin dynamics in solid state materials. Typically, a Fresnel prism is used as a quarter wave plate for terahertz waves to switch linear polarization to circular polarization [95]. The introduced material absorption and Fresnel loss limit the bandwidth and intensity of terahertz waves. The latest advances in plasma based terahertz sources [34,36,37,77–79,82,96–100] have made it possible to observe and even control linear polarization state of intense and broadband terahertz waves through a coherent manipulation of the motion of ionized electron electrically [98,101,102] or optically [103,104]. In all these experiments, the trajectory of released electrons, which contribute to the terahertz polarization state, is determined by the direction of the external field or the relative phase of two-colored optical fields. Although an imperfection of terahertz polarization state such as elliptical polarization from these plasma sources has been reported, insightful physical and theoretical explanation are required for further polarization control and manipulation.

In this section, we present a combined theoretical and experimental study of elliptical polarization properties of generated terahertz waves from laser-induced plasma with a pair of double helix electrodes. We demonstrate that temporal propagation effects are indispensable for understanding the terahertz wave generation process and influence the terahertz polarization substantially. In both experiments and simulations, we observe a remarkable properties change of the elliptical terahertz polarization state with various electrodes design. Such ellipticity is a result of a sensitive dependence of the velocity mismatch between propagation of the optical pulses and generated terahertz pulses. Extensive numerical simulations were performed combining transient current model with pulse velocity retardation, which includes the longitudinal propagation effects responsible for polarization control of terahertz waves.

5.2 Physical mechanism

In the laser-induced ionization process, electrons released from molecules or atoms exhibit a net drifting current after passage of the laser pulses when they experience an asymmetric electrical field [78]. This drifting current, which contributes to the far-field terahertz radiation, is aligned with the direction of an external DC field or asymmetric optical field [102–104]. In our experiment with a pair of double helix electrodes, during the travel of the ionization front, which associates with the propagation of intense laser pulses, the induced net electron current is revolving along the filament due to the longitudinal variation of applied DC electrical field. Furthermore, due to the velocity mismatch between terahertz wave and optical beam, we find that the produced terahertz wave will travel ahead of optical excitation, which will eventually lead to a phase difference between the produced s and p components of terahertz pulse in the far field due to the retarded radiation. We demonstrate that the terahertz polarization state can be coherently manipulated by varying the electrode design and longitudinal properties

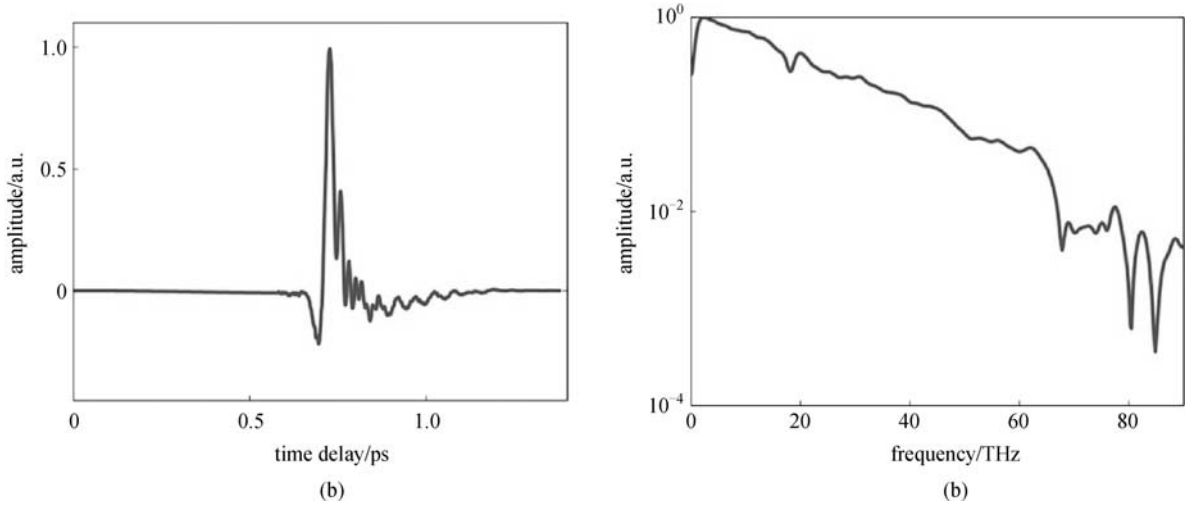

Fig. 29 Measured (a) waveform and (b) corresponding spectrum in ABCD with short pulses. Pulse duration is estimated to be around 15 fs

of plasma. For example, the handedness can be controlled directly through the control of handedness of electrodes and the ellipticity can be controlled by electrodes design.

A theoretical model was built to explain all observed phenomenon. When applying an external bias field on plasma, the driven motion of electrons inside plasma will result in a far-field terahertz radiation, whose polarization is aligned to the external electrical field direction. The plasma can be described by electron density $\rho(t)$, which satisfies $\frac{\partial\rho(t)}{\partial t} = W_{\mathrm{ST}}(t)\left(\rho_0 - \rho(t)\right)$ [97], where ρ_0 is the molecular gas density. $W_{\mathrm{ST}}(t)$ is the ionization rate calculated from static tunneling model, which can be written as

$$W_{\mathrm{ST}}(t) = \frac{\alpha}{\widehat{E}_\omega(t)}\exp\left(-\frac{\beta}{\widehat{E}_\omega(t)}\right),$$

where $\widehat{E}_\omega(t) = E_\omega(t)/E_{\mathrm{a}}$ is the electrical field of fundamental beam in atomic units, $E_{\mathrm{a}} = m^2e^5/(4\pi\varepsilon_0)^3\hbar^4$, $\alpha = 4\omega_{\mathrm{a}}r_{\mathrm{H}}^{5/2}$, $\beta = 2r_{\mathrm{H}}^{3/2}/3$, $\omega_{\mathrm{a}} = me^4/(4\pi\varepsilon_0)^2\hbar^3$, and $r_{\mathrm{H}} = U/U_H$ is the relative molecular ionization potential normalized with that of hydrogen. m, e is the electron mass and charge, respectively. Here, the direction of applied electrical field is alternating along the plasma, which can be expressed as

$$\vec{E}_{\mathrm{DC}}(z) = E_0\cos(\Omega z)\,\vec{x} \pm E_0\sin(\Omega z)\,\vec{y},$$

where E_0 is the amplitude of electrical field, $\Omega = 2\pi/L$ is the alternating frequency which is related to the pitch length of electrodes L, the sign of second term is determined by the handedness.

Considering the averaged collision time of electron with ion τ,

$$\vec{v}(z,t,t_0) = -\frac{e}{m}\int_{t_0}^{t}\left[\vec{E}_{\mathrm{DC}}(z) + \vec{E}_\omega(z,t')\right]H(t'-\tau)\mathrm{d}t',$$

shows the velocity of electrons born at time $t = t_0$, where $H(t'-\tau)$ is the Heaviside function used to describe electron collision.

The transient current which corresponding to terahertz radiation is

$$\vec{J}(z,t) = e\int_{-\infty}^{t}\vec{v}(z,t,t_0)\dot{\rho}(t_0)\mathrm{d}t_0. \tag{44}$$

We used the retarded solution for one-dimensional Maxwell equation

$$\vec{A}(t) = \frac{\mu_0}{4\pi R}\int\vec{J}(z,t)\mathrm{e}^{\mathrm{i}k_{\mathrm{THz}}(R-z)}\mathrm{d}z \tag{45}$$

to describe the longitudinal propagation effect on far-field terahertz radiation pattern. $\vec{A}(t)$ is the vector potential for terahertz waves, μ_0 is the vacuum permeability, R is the distance from origin to field point position z, $k_{\mathrm{THz}} = \omega_{\mathrm{THz}}/v_{\mathrm{THz}}$ is the wave number, ω is the angular frequency of terahertz waves and v_{THz} is the speed of terahertz waves in air .

The constructed far-field terahertz radiation is

$$\vec{E}_{\mathrm{THz}}(t) \propto \frac{\mathrm{e}^{\mathrm{i}kR}}{R}\int_{-L/2}^{L/2}\frac{\partial\vec{J}(z,\omega t - k_{\mathrm{opt}}z)}{\partial t}\mathrm{e}^{-\mathrm{i}k_{\mathrm{THz}}z}\mathrm{d}z, \tag{46}$$

where $\omega t - k_{\mathrm{opt}}z$ describes the propagation of optical pulses in air.

In Eq. (46), obviously, the mismatch between k_{opt} and k_{THz} will contribute to the vector properties of far-field terahertz radiation. We modeled the dynamic process under our experimental condition by considering a focused Gaussian beam, whose peak value along z-axis can be

expressed as

$$E_\omega(z,t) = E_\omega \frac{w_0}{w(z)} \exp(-2t^2/\tau_0^2).$$

$w(z) = w_0[1 + (\lambda z/\pi w_0^2)^2]^{1/2}$ represents the optical field distribution along z axis, w_0 is the beam waist, and λ is the wavelength.

5.3 Experimental setup

A Ti-sapphire amplified laser system, which can deliver laser pulses of 40 fs and 3 mJ at a repetition rate of 1 kHz, is used in this experiment. The laser pulses were split into pump beam and probe beam by a 95% to 5% beam splitter. The optical pump beam was focused by a lens with 400 mm focal length to produce an ionization region with more than 40 mm length in air. Figure 30 shows the illustration of revolving electrical field and a laboratory coordinate. A pair of double helix electrodes, which is made from two copper wires with a 1 mm diameter, was mounted along the plasma region. The two copper wires were twisted for only one pitch along the grooves on a plastic mount, which has an inner diameter of 4 mm and an outer diameter of 6 mm. The inter spacing is around 5 mm and one pitch is 30 mm. The pitch length was chosen to optimize the elipticity of produced terahertz waves under current experimental condition. The bias field was provided by a high voltage modulator, which delivers bipolar square waves with a frequency of 500 Hz and tunable amplitude up to 3 kV. The generated terahertz wave was collected by a 90° off-axis parabolic mirror and then focused again by another parabolic mirror. A 1 mm thick high resistivity silicon wafer was inserted between two parabolic mirrors to block the residue optical beam. The optical probe beam went through a time delay stage and then was focused by a lens with 150 mm focal length through a hole on second parabolic mirror onto a 1 mm thick (110) ZnTe crystal to resolve the temporal information of terahertz waves. To analyze the polarization of terahertz waves, a wired grid terahertz polarizer was used in the collimated terahertz beam path. A combination of a half wave plate and a polarizer was inserted into the optical pump and probe beam to rotate the polarization of the pump and probe beams. Figure 30 also provides the information about our laboratory coordinate. The x- and y-axis represent p and s polarizations, respectively. Note that the applied electrical field originates along the x-axis in laboratory coordinate and revolves clockwise or anti-clockwise depending on the handedness.

5.4 Results and discussion

To clarify the effect related to pump beam polarization, we performed initial measurements by rotating the polarization of pump beam using a half wave plate, which is not shown here. The variation of the peak-to-peak amplitude of the p component of terahertz radiation is independent on pump beam polarization, which is also confirmed in Ref. [98].

An elliptically polarized wave can be resolved into an arbitrary set of mutually orthogonal component waves with their polarization perpendicular to each other and with a fixed phase change. By recomposing the terahertz electric fields obtained at two orthogonal directions, it is feasible to derive the elliptical trajectories if the terahertz pulse is elliptically polarized. In our experiment, the polarization of terahertz waves was obtained by composing the terahertz electric fields in two orthogonal directions measured by

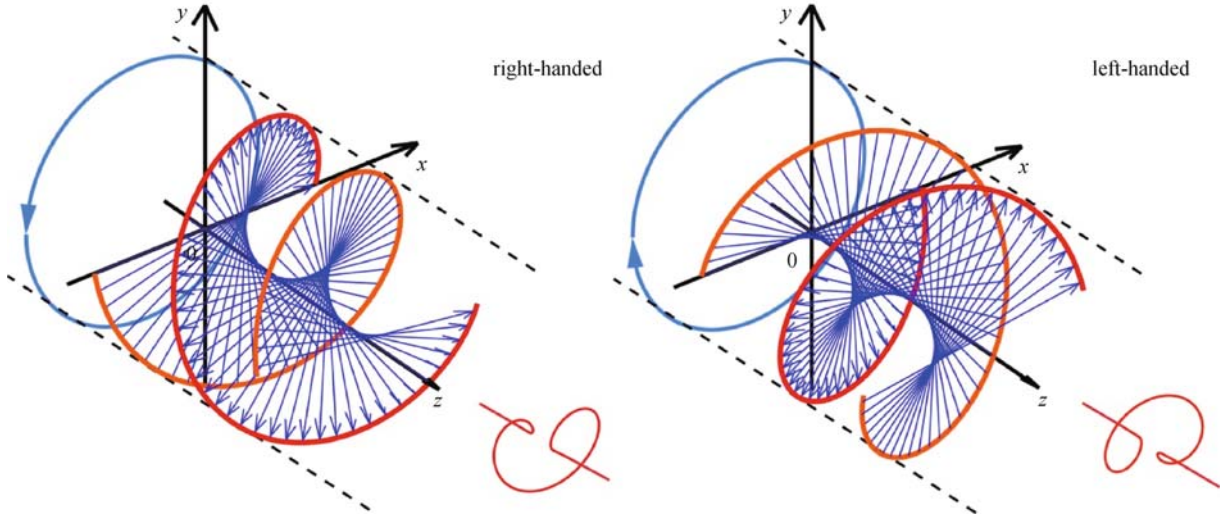

Fig. 30 Illustration of double helix electrical field applied on plasma region. Laser pulses are focused to ionize air where a pair of double helix electrodes was positioned. The trajectory of electrons follows the direction of external electrical field, resulting in an elliptically polarized terahertz wave in far field. The laboratory coordinate and definition of handedness are shown in the figure

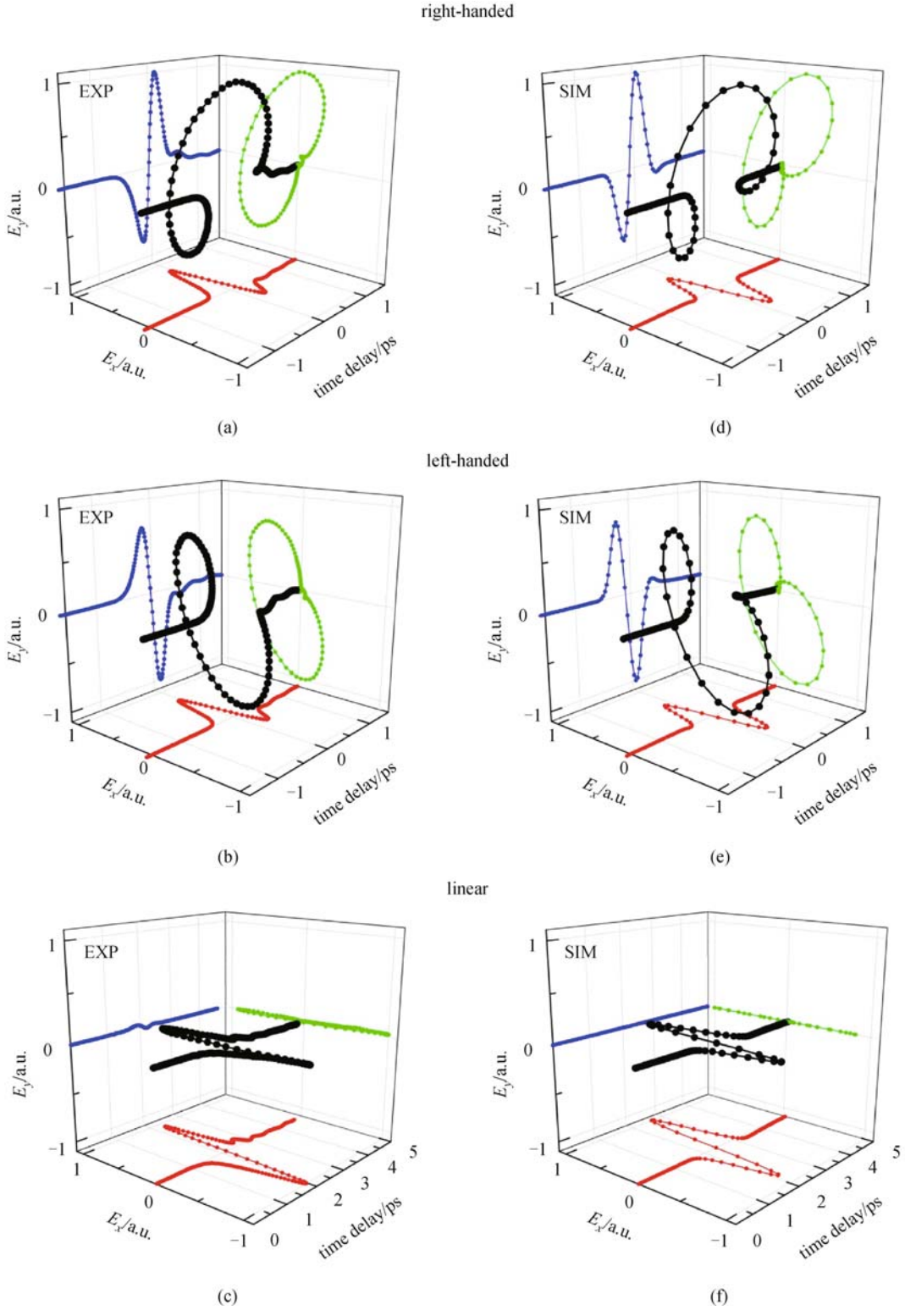

Fig. 31 Temporal evolution of electrical field vector of (a) right-handed and (b) left-handed elliptically polarized and (c) linear polarized terahertz pulses. Simulated temporal evolution of electrical field vector of (d) right-handed and (e) left-handed elliptically polarized and (f) linear polarized terahertz pulses. EXP: experimental results. SIM: simulation results

EO sampling technique, which is shown in Fig. 31. An elliptical terahertz polarization trajectory with an ellipticity $e = 0.5$ was observed on x-y plane in Figs. 31(a) and 31(b). In the presence of the external helical electrical field, the

handedness of elliptically polarized terahertz waves can be manipulated by the longitudinally revolving the direction of DC field. A terahertz wave generated from a pair of linear electrodes is also shown in Fig. 31(c) for comparison.

In our experiment, we measured this velocity mismatch from difference in index of refraction $\Delta n = n_{\text{opt}} - n_{\text{THz}} = 1.08 \times 10^{-4}$ and used this number in all our simulations. Here, we ignore the individual air dispersion effect for optical pulses or terahertz pulses and only consider the relative dispersion between them. Due to the velocity mismatch between optical pulses and terahertz pulses during propagation, within the coherent length, the constructed far-field radiation shows the arbitrary elliptical polarization. The simulated results for various electrodes are shown in Figs. 31(d)–31(f) for comparison. The simulated results agree well with experimental findings and also, depending on the revolving direction of electrical field, the polarization of output terahertz pulse demonstrates a controllable handedness.

Moreover, one interesting phenomenon is related to longitudinal symmetry of plasma density and the pitch length of applied electrical field. We noted that as we move the electrodes away from the center of the plasma, the constructed far-field terahertz radiation shows different ellipticity. To demonstrate the effects associated with plasma profile, Figs. 32(a) and 32(b) shows a series of measured x and y components of terahertz field while moving electrodes position along plasma with right-handed and left-handed electrodes, respectively. A case with linear electrodes is also shown in Fig. 32(c) for comparison. The theoretical calculated results are also shown in Figs. 32(d)–32(f) with corresponding condition of applied electrical field. The black curves reveal the polarization properties of far-field terahertz radiation at various positions, which defines as the relatively position between the centers of plasma and the electrodes. We found that, in our method, the property of far-field terahertz polarization depends not only with applied electrical field, but also with the uniformity of plasma.

To clarify elliptically polarized terahertz waves generated from double helix electrodes, we compared the results with that obtained by a Fresnel prism made of high-density polyethylene (HDPE). Figures 33(a) and 33(b) plot the electric vector of right-handed and left-handed circularly polarized terahertz wave obtained with the Fresnel prism, respectively. The input terahertz polarization was controlled by a terahertz polarizer. Two main characters of circular or elliptical polarized beam are amplitude ratio E_x/E_y and phase difference $\phi_x - \phi_y$ between x and y components. For a perfect circularly polarized broadband pulses, $E_x(\omega)/E_y(\omega) = 1$ and $\phi_x(\omega) - \phi_y(\omega) = \pm\pi/2$ hold for all the frequencies. We extracted the amplitude ratio and the phase difference between x and y components through Fourier transform of experimental data and plotted in Figs. 33(c) – 33(f) for each case. Due to the large index of refraction and absorption of HDPE, the E_x/E_y and $\phi_x - \phi_y$ have a relatively large fluctuation around optimized number. As contrast, with double helix electrodes, especially at the position around the center of the plasma, the phase difference and amplitude ratio have minimum fluctuation across the spectral range, providing an elliptical polarized terahertz wave.

To produce a nearly circularly polarized terahertz waves through our method, the plasma longitudinal profile and the pitch length are two principle factors. From the above discussion, it is obvious that E_x/E_y of produced terahertz pulses is related to the plasma longitudinal profile since the generation efficiency is consequentially associated to the plasma density, and $\phi_x - \phi_y$ is strongly dependent on the pitch length of the revolving electrical field since the phase difference is provided from the velocity mismatch. These two factors provide the design parameters of this plasma based circular polarized terahertz sources.

6 Conclusions

This paper reviewed a systematic study of broadband terahertz wave detection with gaseous media, as well as a technological improvement of broadband THz-TDS, which included a balanced detection scheme and a novel elliptical polarization control of broadband terahertz waves.

It starts with the four-wave mixing model of terahertz detection with gaseous media. A complete theory was presented under both plane wave approximation and focused Gaussian beam condition. The optimal conditions for the detection process were derived and explored to demonstrate how a terahertz system with gaseous sensors can be optimized. The experiments under different probe pulse energy, biased field strength, nonlinear susceptibility of gases, gas pressure, and laser pulse duration were systematically performed to verify the analytical model and further optimize the sensitivity and efficiency of the terahertz wave gaseous sensor. A figure of merit was defined to identify an efficient gaseous sensor. Compared to the nitrogen gas, *n*-butane had been demonstrated to achieve a factor of 240 improvement of dynamic range under the same condition. Moreover, an ultra-broadband terahertz wave detection covering up to 70 THz was achieved with sub-20 fs laser pulses delivered from a hollow-core fiber pulse compressor.

Inspired by the balanced detection with electro-optic crystals, we further introduced a balanced detection scheme for ABCD to reduce the common noise from laser fluctuation. When the polarization of terahertz waves, laser probe beam, and the direction of bias field were oriented at a certain angle, utilizing third-order nonlinear susceptibility tensor elements of gases, second harmonic

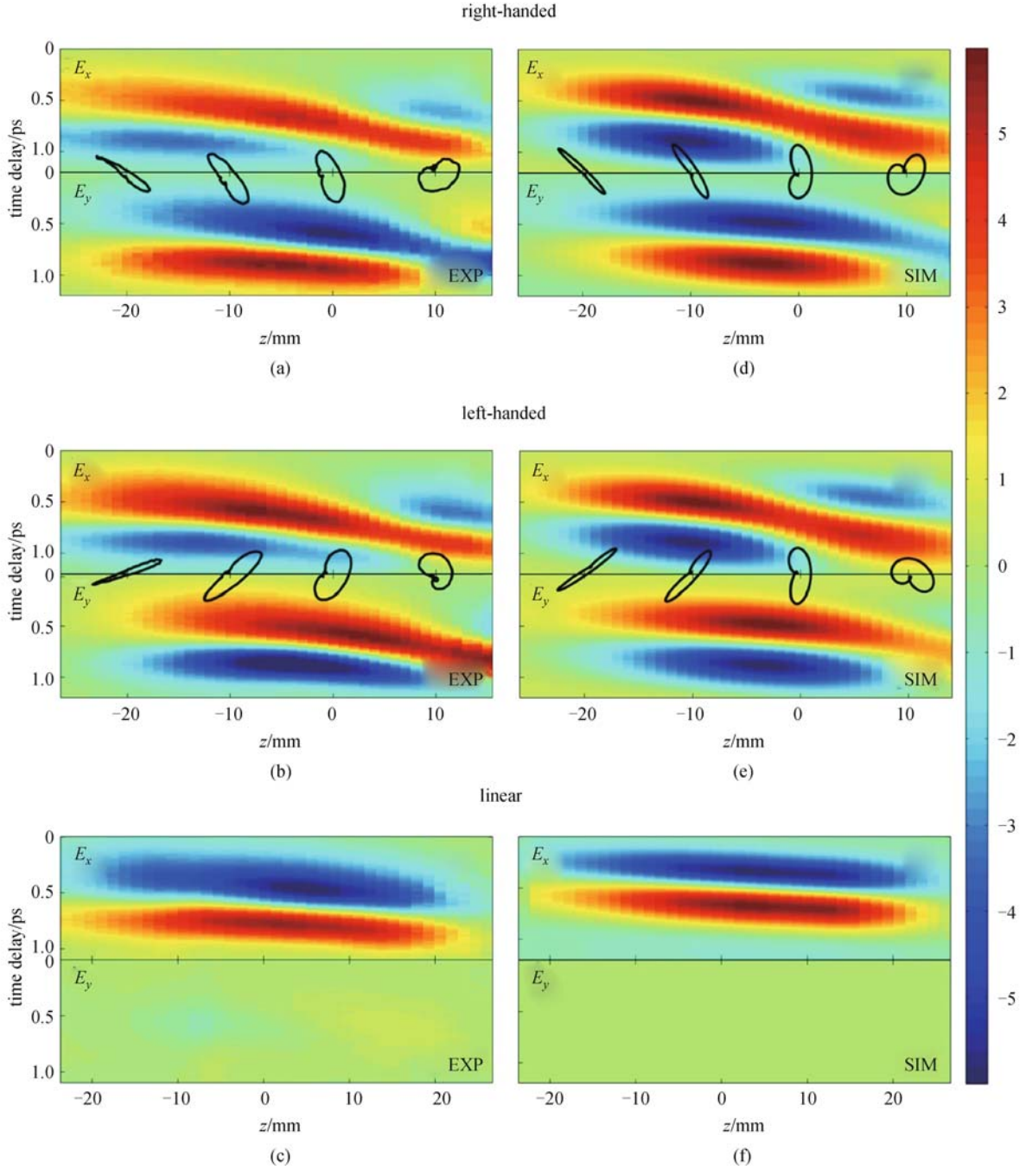

Fig. 32 Measured far-field terahertz waves in x (upper) and y (lower) direction at various electrodes position from pairs of (a) right-handed; (b) left-handed helical and (c) linear electrodes. The calculated far-field terahertz waves in x and y direction at various electrodes position from (d) right-handed and (e) left-handed helical and (f) linear electrodes are also shown for comparison. Black curves show the polarization trajectories of far-field terahertz radiation at position z = –20, –10, 0, 10 mm, respectively. EXP: experimental results. SIM: simulation results

photons with both orthogonal polarizations were produced simultaneously. The differential signal between two orthogonally polarized second harmonic photons reduced the correlated noise in the balanced detection geometry and greatly improved the signal-to-noise ratio and dynamic range of the system. A factor of two improvement of signal-to-noise ratio was demonstrated experimentally.

In the last part of this paper, we demonstrated that the

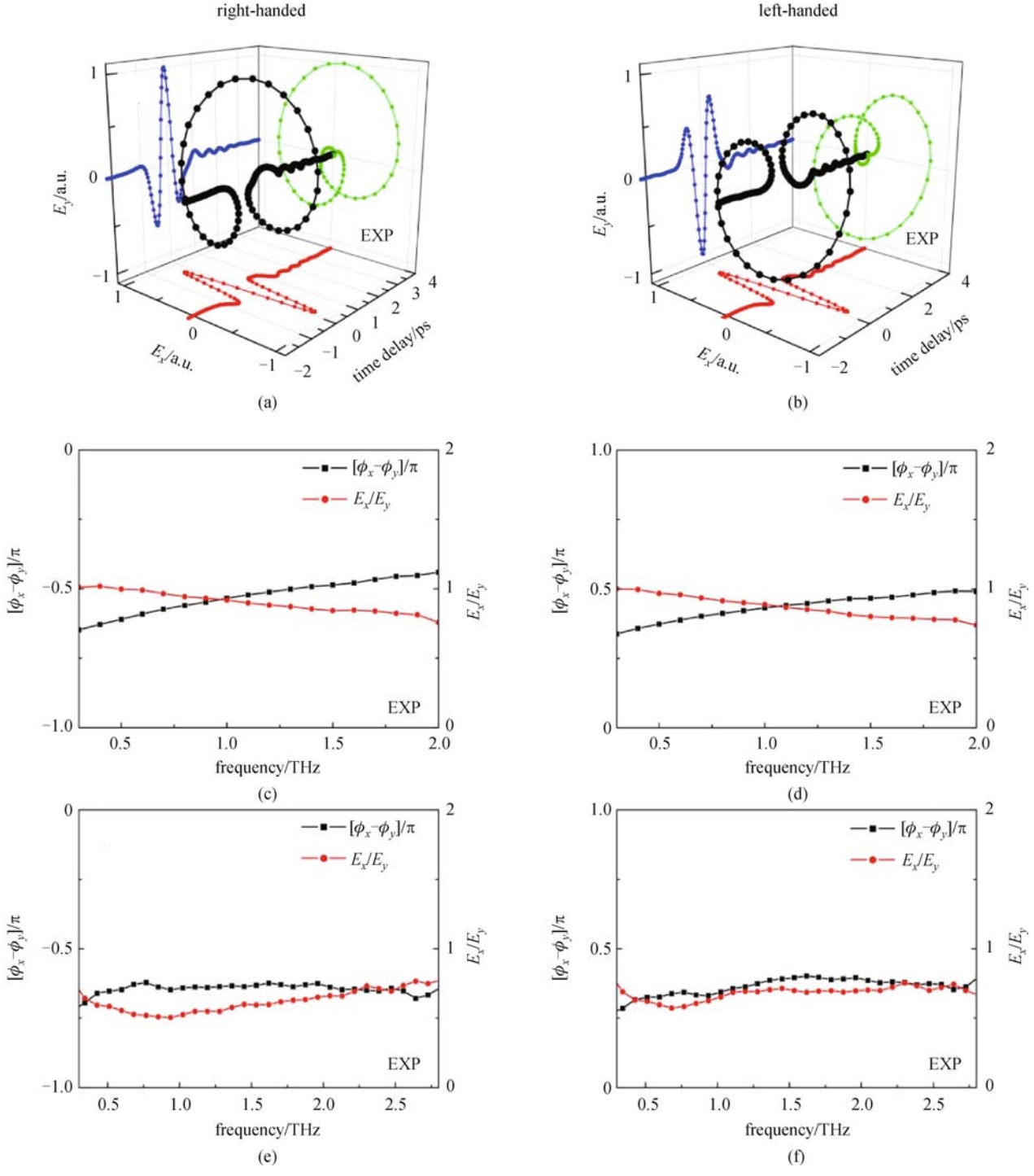

Fig. 33 Measured temporal evolution of electrical field vector of (a) right-handed and (b) left-handed circular polarized terahertz pulses with a HDPE Fresnel prism. The phase difference and amplitude ratio between *x* and *y* component for (c) right-handed and (d) left-handed circular polarized terahertz pulses in frequency domain; (e) phase difference and (f) amplitude ratio of elliptically polarized terahertz pulses generated from double helix electrodes are shown for comparison. EXP: experimental results

polarization of far-field terahertz radiation can be significantly modified through manipulation of revolving electron transient current in laser filament with a pair of double helix electrodes. An elliptically polarized far-field terahertz wave pattern was observed and demonstrated to be highly sensitive to the handedness of applied electrical field and position of electrodes. The velocity mismatch between optical excitation and propagation of terahertz

waves was verified to be the underlying mechanism. This finding provides new perception of plasma-based terahertz emitters, opens interesting perspectives to coherently control polarization properties of terahertz emission in a broader spectral range, and offers a useful diagnostics tool for biomolecular and spintronics study in the terahertz frequency.

In summary, this paper provides an improved understanding of the terahertz ABCD process and experimental results that optimize the capabilities of broadband THz-TDS systems based on them. Broadband THz-TDS will further help to benefit the terahertz community and open interdisciplinary research areas. Especially in ultrafast laser science, broadband terahertz time domain spectroscopy provides a useful tool to probe ultrafast phenomenon and to investigate time-resolved dynamic in materials.

Acknowledgements This work was supported in part by the Army Research Office-Multidisciplinary University Research Initiative (ARO-MURI), Defense Threat Reduction Agency (DTRA), and the National Natural Science Foundation (NSF) of China, and Wuhan National Laboratory for Optoelectronics in Huazhong University of Science and Technology.

References

1. Ferguson B, Zhang X C. Materials for terahertz science and technology. Nature Materials, 2002, 1(1): 26–33
2. Siegel P H. Terahertz technology. IEEE Transactions on Microwave Theory and Techniques, 2002, 50(3): 910–928
3. Tonouchi M. Cutting-edge terahertz technology. Nature Photonics, 2007, 1(2): 97–105
4. Nuss M, Orenstein J. Terahertz time-domain spectroscopy. In: Grüner G, ed. Millimeter and Submillimeter Wave Spectroscopy of Solids. Berlin/Heidelberg: Springer, 1998, 7–50
5. Grischkowsky D, Keiding S, Exter M, Fattinger C. Far-infrared time-domain spectroscopy with terahertz beams of dielectrics and semiconductors. Journal of the Optical Society of America. B, Optical Physics, 1990, 7(10): 2006–2015
6. Exter M, Fattinger C, Grischkowsky D. Terahertz time-domain spectroscopy of water vapor. Optics Letters, 1989, 14(20): 1128–1130
7. Yeh K L, Hoffmann M C, Hebling J, Nelson K A. Generation of 10 μJ ultrashort terahertz pulses by optical rectification. Applied Physics Letters, 2007, 90(17): 171121
8. You D, Jones R R, Bucksbaum P H, Dykaar D R. Generation of high-power sub-single-cycle 500-fs electromagnetic pulses. Optics Letters, 1993, 18(4): 290–292
9. Bartel T, Gaal P, Reimann K, Woerner M, Elsaesser T. Generation of single-cycle THz transients with high electric-field amplitudes. Optics Letters, 2005, 30(20): 2805–2807
10. Hirori H, Doi A, Blanchard F, Tanaka K. Single-cycle terahertz pulses with amplitudes exceeding 1 MV/cm generated by optical rectification in $LiNbO_3$. Applied Physics Letters, 2011, 98(9): 091106
11. Sell A, Leitenstorfer A, Huber R. Phase-locked generation and field-resolved detection of widely tunable terahertz pulses with amplitudes exceeding 100 MV/cm. Optics Letters, 2008, 33(23): 2767–2769
12. Cao J C. Interband impact ionization and nonlinear absorption of terahertz radiation in semiconductor heterostructures. Physical Review Letters, 2003, 91(23): 237401
13. Gaal P, Reimann K, Woerner M, Elsaesser T, Hey R, Ploog K H. Nonlinear terahertz response of -type GaAs. Physical Review Letters, 2006, 96(18): 187402
14. Danielson J R, Lee Y S, Prineas J P, Steiner J T, Kira M, Koch S W. Interaction of strong single-cycle terahertz pulses with semiconductor quantum wells. Physical Review Letters, 2007, 99 (23): 237401
15. Shen Y, Watanabe T, Arena D A, Kao C C, Murphy J B, Tsang T Y, Wang X J, Carr G L. Nonlinear cross-phase modulation with intense single-cycle terahertz pulses. Physical Review Letters, 2007, 99(4): 043901
16. Su F H, Blanchard F, Sharma G, Razzari L, Ayesheshim A, Cocker T L, Titova L V, Ozaki T, Kieffer J C, Morandotti R, Reid M, Hegmann F A. Terahertz pulse induced intervalley scattering in photoexcited GaAs. Optics Express, 2009, 17(12): 9620–9629
17. Jewariya M, Nagai M, Tanaka K. Ladder climbing on the anharmonic intermolecular potential in an amino acid microcrystal via an intense monocycle terahertz pulse. Physical Review Letters, 2010, 105(20): 203003
18. Kuehn W, Gaal P, Reimann K, Woerner M, Elsaesser T, Hey R. Coherent ballistic motion of electrons in a periodic potential. Physical Review Letters, 2010, 104(14): 146602
19. Kampfrath T, Sell A, Klatt G, Pashkin A, Mahrlein S, Dekorsy T, Wolf M, Fiebig M, Leitenstorfer A, Huber R. Coherent terahertz control of antiferromagnetic spin waves. Nature Photonics, 2011, 5 (1): 31–34
20. Leinß S, Kampfrath T, Volkmann K, Wolf M, Steiner J T, Kira M, Koch S W, Leitenstorfer A, Huber R. Terahertz coherent control of optically dark paraexcitons in Cu_2O. Physical Review Letters, 2008, 101(24): 246401
21. Huber R, Tauser F, Brodschelm A, Bichler M, Abstreiter G, Leitenstorfer A. How many-particle interactions develop after ultrafast excitation of an electron-hole plasma. Nature, 2001, 414 (6861): 286–289
22. Kaindl R A, Carnahan M A, Hägele D, Lövenich R, Chemla D S. Ultrafast terahertz probes of transient conducting and insulating phases in an electron-hole gas. Nature, 2003, 423(6941): 734–738
23. Günter G, Anappara A A, Hees J, Sell A, Biasiol G, Sorba L, De Liberato S, Ciuti C, Tredicucci A, Leitenstorfer A, Huber R. Sub-cycle switch-on of ultrastrong light-matter interaction. Nature, 2009, 458(7235): 178–181
24. Hu B B, Zhang X C, Auston D H, Smith P R. Free-space radiation from electrooptic crystals. Applied Physics Letters, 1990, 56(6): 506–508
25. Han P Y, Zhang X C. Free-space coherent broadband terahertz time-domain spectroscopy. Measurement Science & Technology, 2001, 12(11): 1747–1756
26. Huber R, Brodschelm A, Tauser F, Leitenstorfer A. Generation and field-resolved detection of femtosecond electromagnetic pulses

tunable up to 41 THz. Applied Physics Letters, 2000, 76(22): 3191–3193
27. Kübler C, Huber R, Tubel S, Leitenstorfer A. Ultrabroadband detection of multi-terahertz field transients with GaSe electro-optic sensors: approaching the near infrared. Applied Physics Letters, 2004, 85(16): 3360–3362
28. Auston D H. Picosecond optoelectronic switching and gating in silicon. Applied Physics Letters, 1975, 26(3): 101–103 doi:10.1063/1.88079
29. Mourou G, Stancampiano C V, Antonetti A, Orszag A. Picosecond microwave pulses generated with a subpicosecond laser-driven semiconductor switch. Applied Physics Letters, 1981, 39(4): 295–296
30. Fattinger C, Grischkowsky D. Point source terahertz optics. Applied Physics Letters, 1988, 53(16): 1480–1482
31. Krökel D, Grischkowsky D, Ketchen M B. Subpicosecond electrical pulse generation using photoconductive switches with long carrier lifetimes. Applied Physics Letters, 1989, 54(11): 1046–1047
32. Shen Y C, Upadhya P C, Linfield E H, Beere H E, Davies A G. Ultrabroadband terahertz radiation from low-temperature-grown GaAs photoconductive emitters. Applied Physics Letters, 2003, 83 (15): 3117–3119
33. Fill E, Borgström S, Larsson J, Starczewski T, Wahlström C G, Svanberg S. XUV spectra of optical-field-ionized plasmas. Physical Review E: Statistical Physics, Plasmas, Fluids, and Related Interdisciplinary Topics, 1995, 51(6): 6016–6027
34. Hamster H, Sullivan A, Gordon S, White W, Falcone R W. Subpicosecond, electromagnetic pulses from intense laser-plasma interaction. Physical Review Letters, 1993, 71(17): 2725–2728
35. Forestier B, Houard A, Durand M, Andre Y B, Prade B, Dauvignac J Y, Perret F, Pichot C, Pellet M, Mysyrowicz A. Radiofrequency conical emission from femtosecond filaments in air. Applied Physics Letters, 2010, 96(14): 141111
36. Cook D J, Hochstrasser R M. Intense terahertz pulses by four-wave rectification in air. Optics Letters, 2000, 25(16): 1210–1212
37. Thomson M D, Blank V, Roskos H G. Terahertz white-light pulses from an air plasma photo-induced by incommensurate two-color optical fields. Optics Express, 2010, 18(22): 23173–23182
38. Wu Q, Zhang X C. Free-space electro-optics sampling of mid-infrared pulses. Applied Physics Letters, 1997, 71(10): 1285–1286
39. Jepsen P U, Winnewisser C, Schall M, Schyja V, Keiding S R, Helm H. Detection of THz pulses by phase retardation in lithium tantalate. Physical Review E: Statistical Physics, Plasmas, Fluids, and Related Interdisciplinary Topics, 1996, 53(4): R3052–R3054
40. Nahata A, Auston D H, Heinz T F, Wu C. Coherent detection of freely propagating terahertz radiation by electro-optic sampling. Applied Physics Letters, 1996, 68(2): 150–152
41. Vagelatos N, Wehe D, King J S. Phonon dispersion and phonon densities of states for ZnS and ZnTe. Journal of Chemical Physics, 1974, 60(9): 3613–3618
42. Kleinman D A, Spitzer W G. Infrared lattice absorption of GaP. Physical Review, 1960, 118(1): 110–117
43. Gupta S, Frankel M Y, Valdmanis J A, Whitaker J F, Mourou G A, Smith F W, Calawa A R. Subpicosecond carrier lifetime in GaAs grown by molecular beam epitaxy at low temperatures. Applied Physics Letters, 1991, 59(25): 3276–3278
44. Prabhu S S, Ralph S E, Melloch M R, Harmon E S. Carrier dynamics of low-temperature-grown GaAs observed via THz spectroscopy. Applied Physics Letters, 1997, 70(18): 2419–2421
45. Kono S, Tani M, Sakai K. Coherent detection of mid-infrared radiation up to 60 THz with an LT-GaAs photoconductive antenna. Iee P-Optoelectron, 2002, 149(3): 105–109
46. Liu J, Zhang X C. Terahertz-radiation-enhanced emission of fluorescence from gas plasma. Physical Review Letters, 2009, 103 (23): 235002
47. Liu J, Zhang X C. Plasma characterization using terahertz-wave-enhanced fluorescence. Applied Physics Letters, 2010, 96(4): 041505
48. Liu J, Dai J, Chin S L, Zhang X C. Broadband terahertz wave remote sensing using coherent manipulation of fluorescence from asymmetrically ionized gases. Nature Photonics, 2010, 4(9): 627–631
49. Clough B, Liu J, Zhang X C. Laser-induced photoacoustics influenced by single-cycle terahertz radiation. Optics Letters, 2010, 35(21): 3544–3546
50. Liu J, Clough B, Zhang X C. Enhancement of photoacoustic emission through terahertz-field-driven electron motions. Physical Review E: Statistical, Nonlinear, and Soft Matter Physics, 2010, 82 (6 Pt 2): 066602
51. Dai J, Xie X, Zhang X C. Detection of broadband terahertz waves with a laser-induced plasma in gases. Physical Review Letters, 2006, 97(10): 103903
52. Karpowicz N, Dai J, Lu X, Chen Y, Yamaguchi M, Zhao H, Zhang X C, Zhang L, Zhang C, Price-Gallagher M, Fletcher C, Mamer O, Lesimple A, Johnson K. Coherent heterodyne time-domain spectrometry covering the entire “terahertz gap”. Applied Physics Letters, 2008, 92(1): 011131
53. Nahata A, Heinz T F. Detection of freely propagating terahertz radiation by use of optical second-harmonic generation. Optics Letters, 1998, 23(1): 67–69
54. Cook D J, Chen J X, Morlino E A, Hochstrasser R M. Terahertz-field-induced second-harmonic generation measurements of liquid dynamics. Chemical Physics Letters, 1999, 309(3–4): 221–228
55. Lu X, Karpowicz N, Zhang X C. Broadband terahertz detection with selected gases. Journal of the Optical Society of America. B, Optical Physics, 2009, 26(9): A66–A73
56. Lu X, Zhang X C.Terahertz wave gas photonics: sensing with gases. Journal of Infrared, Millimeter and Terahertz Waves, 2011, 32(5): 562–569
57. Lu X, Karpowicz N, Chen Y, Zhang X C. Systematic study of broadband terahertz gas sensor. Applied Physics Letters, 2008, 93 (26): 261106
58. Kleinman D A, Ashkin A, Boyd G D. Second-harmonic generation of light by focused laser beams. Physical Review, 1966, 145(1): 338
59. Ward J F, New G H C. Optical third harmonic generation in gases by a focused laser beam. Physical Review, 1969, 185(1): 57
60. Karpowics N. Physics and utilization of terahertz gas photonics. In: Physics. Rensselaer Polytechnic Institute, Troy, NY, 2009, 124

61. Finn R S, Ward J F. DC-induced optical second-harmonic generation in the inert gases. Physical Review Letters, 1971, 26: 285–289
62. Becker A, Akozbek N, Vijayalakshmi K, Oral E, Bowden C M, Chin S L. Intensity clamping and re-focusing of intense femtosecond laser pulses in nitrogen molecular gas. Applied Physics. B, Lasers and Optics, 2001, 73(3): 287–290
63. Shelton D P. Nonlinear-optical susceptibilities of gases measured at 1064 and 1319 nm. Physical Review A, 1990, 42(5): 2578–2592 PMID:9904326
64. Boyd R W. Nonlinear Optics. Burlington, MA: Academic Press, 2008
65. Hermann J P, Ducuing J. Third-order polarizabilities of long-chain molecules. Journal of Applied Physics, 1974, 45(11): 5100–5102
66. Rustagi K C, Ducuing J. Third-order optical polarizability of conjugated organic-molecules. Optics Communications, 1974, 10 (3): 258–261
67. Korff S, Breit G. Optical dispersion. Reviews of Modern Physics, 1932, 4(3): 471–503
68. Gouy L G. Sur la propagation anomale des ondes. Compt. Rendue Acad. Sci. Paris, 1890, 111: 33
69. Gouy L G. Sur une propriete nouvelle des ondes lumineuses. C. R. Acad. Sci. Paris, 1890, 110: 1251
70. Ruffin A B, Rudd J V, Whitaker J F, Feng S, Winful H G. Direct observation of the Gouy phase shift with single-cycle terahertz pulses. Physical Review Letters, 1999, 83(17): 3410–3413
71. Lide D R, ed. CRC Handbook of Chemistry and Physics. 86th ed. Boca Raton: CRC-Press, 2005
72. Wu Q, Zhang X C. Free-space electro-optics sampling of mid-infrared pulses. Applied Physics Letters, 1997, 71(10): 1285–1286
73. Naftaly M, Dudley R. Methodologies for determining the dynamic ranges and signal-to-noise ratios of terahertz time-domain spectrometers. Optics Letters, 2009, 34(8): 1213–1215
74. Bigio I J, Ward J F. Measurement of the hyperpolarizability ratio $\chi_{yyyy}(-2\omega;\ 0,\ \omega,\ \omega)/\chi_{yyxx}(-2\omega;\ 0,\ \omega,\ \omega)$ for the inert gases. Physical Review A, 1974, 9(1): 35–39
75. Ward J F, Bigio I J. Molecular second- and third-order polarizabilities from measurements of second-harmonic generation in gases. Physical Review A, 1975, 11(1): 60–66
76. Ward J F, Miller C K. Measurements of nonlinear optical polarizabilities for twelve small molecules. Physical Review A, 1979, 19(2): 826–833
77. Xie X, Dai J, Zhang X C. Coherent control of THz wave generation in ambient air. Physical Review Letters, 2006, 96(7): 075005
78. Kim K Y, Glownia J H, Taylor A J, Rodriguez G. Terahertz emission from ultrafast ionizing air in symmetry-broken laser fields. Optics Express, 2007, 15(8): 4577–4584
79. Kim K Y, Taylor A J, Glownia J H, Rodriguez G. Coherent control of terahertz supercontinuum generation in ultrafast laser-gas interactions. Nature Photonics, 2008, 2(10): 605–609
80. Karpowicz N, Zhang X C. Coherent terahertz echo of tunnel ionization in gases. Physical Review Letters, 2009, 102(9): 093001
81. Silaev A A, Vvedenskii N V. Residual-current excitation in plasmas produced by few-cycle laser pulses. Physical Review Letters, 2009, 102(11): 115005
82. Kreß M, Löffler T, Thomson M D, Dörner R, Gimpel H, Zrost K, Ergler T, Moshammer R, Morgner U, Ullrich J, Roskos H G. Determination of the carrier-envelope phase of few-cycle laser pulses with terahertz-emission spectroscopy. Nature Physics, 2006, 2(5): 327–331
83. Jones D J, Diddams S A, Ranka J K, Stentz A, Windeler R S, Hall J L, Cundiff S T. Carrier-envelope phase control of femtosecond mode-locked lasers and direct optical frequency synthesis. Science, 2000, 288(5466): 635–639
84. Paulus G G, Grasbon F, Walther H, Villoresi P, Nisoli M, Stagira S, Priori E, De Silvestri S. Absolute-phase phenomena in photoionization with few-cycle laser pulses. Nature, 2001, 414(6860): 182–184
85. Ferrari F, Calegari F, Lucchini M, Vozzi C, Stagira S, Sansone G, Nisoli M. High-energy isolated attosecond pulses generated by above-saturation few-cycle fields. Nature Photonics, 2010, 4(12): 875–879
86. Paul P M, Toma E S, Breger P, Mullot G, Augé F, Balcou P, Muller H G, Agostini P. Observation of a train of attosecond pulses from high harmonic generation. Science, 2001, 292(5522): 1689–1692
87. Strickland D, Mourou G. Compression of amplified chirped optical pulses. Optics Communications, 1985, 56(3): 219–221
88. Nisoli M, De Silvestri S, Svelto O. Generation of high energy 10 fs pulses by a new pulse compression technique. Applied Physics Letters, 1996, 68(20): 2793–2795
89. Nisoli M, De Silvestri S, Svelto O, Szipöcs R, Ferencz K, Spielmann C, Sartania S, Krausz F. Compression of high-energy laser pulses below 5 fs. Optics Letters, 1997, 22(8): 522–524
90. Matsubara E, Yamane K, Sekikawa T, Yamashita M. Generation of 2.6 fs optical pulses using induced-phase modulation in a gas-filled hollow fiber. Journal of the Optical Society of America. B, Optical Physics, 2007, 24(4): 985–989
91. Hauri C P, Kornelis W, Helbing F W, Heinrich A, Couairon A, Mysyrowicz A, Biegert J, Keller U. Generation of intense, carrier-envelope phase-locked few-cycle laser pulses through filamentation. Applied Physics. B, Lasers and Optics, 2004, 79(6): 673–677
92. Couairon A, Franco M, Mysyrowicz A, Biegert J, Keller U. Pulse self-compression to the single-cycle limit by filamentation in a gas with a pressure gradient. Optics Letters, 2005, 30(19): 2657–2659
93. Kane D J, Trebino R. Single-shot measurement of the intensity and phase of an arbitrary ultrashort pulse by using frequency-resolved optical gating. Optics Letters, 1993, 18(10): 823–825
94. Johnson F A. Lattice absorption bands in silicon. Proceedings of the Physical Society, London, 1959, 73(2): 265–272
95. Shan J, Dadap J I, Heinz T F. Circularly polarized light in the single-cycle limit: The nature of highly polychromatic radiation of defined polarization. Optics Express, 2009, 17(9): 7431–7439
96. Löffler T, Jacob F, Roskos H G. Generation of terahertz pulses by photoionization of electrically biased air. Applied Physics Letters, 2000, 77(3): 453–455
97. Roskos H G, Thomson M D, Kreß M, Löffler T. Broadband THz emission from gas plasmas induced by femtosecond optical pulses: from fundamentals to applications. Laser Photonics Rev, 2007, 1 (4): 349–368
98. Houard A, Liu Y, Prade B, Tikhonchuk V T, Mysyrowicz A. Strong enhancement of terahertz radiation from laser filaments in air by a static electric field. Physical Review Letters, 2008, 100

(25): 255006

99. Blanchard F, Sharma G, Ropagnol X, Razzari L, Morandotti R, Ozaki T. Improved terahertz two-color plasma sources pumped by high intensity laser beam. Optics Express, 2009, 17(8): 6044–6052
100. Babushkin I, Kuehn W, Köhler C, Skupin S, Bergé L, Reimann K, Woerner M, Herrmann J, Elsaesser T. Ultrafast spatiotemporal dynamics of terahertz generation by ionizing two-color femtosecond pulses in gases. Physical Review Letters, 2010, 105(5): 053903
101. Liu Y, Houard A, Prade B, Mysyrowicz A, Diaw A, Tikhonchuk V T. Amplification of transition-Cherenkov terahertz radiation of femtosecond filament in air. Applied Physics Letters, 2008, 93(5): 051108
102. Chen Y P, Wang T J, Marceau C, Théberge F, Châteauneuf M, Dubois J, Kosareva O, Chin S L. Characterization of terahertz emission from a dc-biased filament in air. Applied Physics Letters, 2009, 95: 101101
103. Dai J, Karpowicz N, Zhang X C. Coherent polarization control of terahertz waves generated from two-color laser-induced gas plasma. Physical Review Letters, 2009, 103(2): 023001
104. Wen H D, Lindenberg A M. Coherent terahertz polarization control through manipulation of electron trajectories. Physical Review Letters, 2009, 103(2): 023902

Xiaofei Lu –Physicist at SunEdison Inc, Saint Peters, MO. She received her Ph.D. in Physics from Rensselaer Polytechnic Institute (RPI), Troy, NY, where she involved in terahertz science and technology under Prof. Xi-Cheng Zhang's guidance. Prior to RPI, she received her B.S. in optoelectronics from Tianjin University, Tianjin, China. In Rensselaer, she contributed to development of broadband terahertz time-domain spectroscope with gases. She authored or co-authored more than ten journal publications and her work was presented in major conferences. She was awarded as a National Science Foundation IGERT Trainee since 2009. She was given the Coherent Award for Outstanding Research Achievement in 2009 and the Rensselaer Founders' Award for Excellence in 2008.

Xi-Cheng Zhang–Parker Givens Chair of Optics, assumes Directorship of The Institute of Optics, University of Rochester (UR), NY, a foremost institution in optics and optical physics research and education, on 1/1/2012. Prior to joining UR, he pioneered world-leading research in the field of ultrafast laser-based terahertz technology and optical physics at Rensselaer Polytechnic Institute (RPI), Troy, NY (1992–2012). At RPI, he is the Eric Jonsson Professor of Science; Acting Head at the Department of Physics, Applied Physics & Astronomy; Professor of Electrical, Computer & System; and Founding Director of the Center for THz Research. He is co-founder of Zomega Terahertz Corp. With a B.S. (1982) from Peking University, he earned the M.S. (1983) and Ph.D. degree (1985) in Physics from Brown University, RI.

Previous positions included Visiting Scientist at MIT (1985), Physical Tech. Division of Amoco Research Center (1987), EE Dept. at Columbia University (1987–1991); Distinguished Visiting Scientist at Jet Propulsion Lab, Caltech (2006). He holds 27 U.S. patents, and is a prolific author and speaker. He is a Fellow of AAAS, APS (lifetime), IEEE, and OSA (lifetime). Dr. Zhang served as Editor-in-Chief of Optics Letters (2014–2016).

His honors and awards include: IRMMW-THz Kenneth Button Prize (2014); OSA William F. Meggers Award (2012); IEEE Photonics Society William Streifer Scientific Achievement Award (2011); Rensselaer William H. Wiley 1866 Award (2009); Japan Society for the Promotion of Science Fellowship & NRC-CIAR Distinguished Visiting Scientist, Ottawa, Canada (2004); and First Heinrich Rudolf Hertz Lecturer, RWTH, Aachen, Germany (2003). He also served two years as a Distinguished Lecturer of IEEE/LEOS. He received Rensselaer Early Career Award (1996), Research Corporation Cottrell Scholar Award (1995), NSF Early Career Award (1995), K.C. Wong Prize, K.C. Wong Foundation, Hong Kong (1995), NSF Research Initiation Award (1992). In 1993–1994, he was an AFOSR-SRPF Fellow at Hanscom Air Force Base.